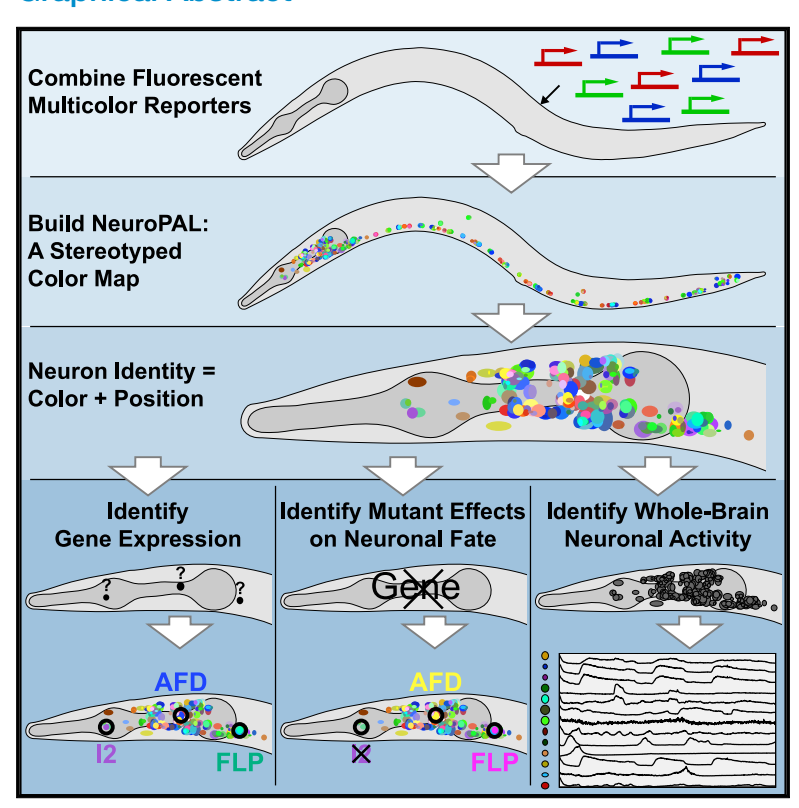


NeuroPAL: A Multicolor Atlas for Whole-Brain Neuronal Identification in *C. elegans*

Graphical Abstract



Authors

Eviatar Yemini, Albert Lin, Amin Nejatbakhsh, ..., Liam Paninski, Vivek Venkatachalam, Oliver Hobert

Correspondence

eiy1@columbia.edu

In Brief

The multicolor transgene NeuroPAL allows for nervous-system-wide neuronal identification in *C. elegans* using a combination of reporters and colors to generate an invariant color map across individuals and is compatible with reporters for gene expression and neuronal activity.

Highlights

- NeuroPAL: a strain with a stereotyped fluorescent color map to identify all neurons
- NeuroPAL and semi-automated ID software pinpoint patterns of reporter gene expression
- NeuroPAL identifies neuronal differentiation defects in mutant backgrounds
- Dynamic whole-brain neuronal activity patterns defined by NeuroPAL in combination with GCaMP









Resource

NeuroPAL: A Multicolor Atlas for Whole-Brain Neuronal Identification in *C. elegans*

Eviatar Yemini, 1,7,* Albert Lin, 2 Amin Nejatbakhsh, 3 Erdem Varol, 3 Ruoxi Sun, 3 Gonzalo E. Mena, 4 Aravinthan D.T. Samuel, 2 Liam Paninski, 3 Vivek Venkatachalam, 5 and Oliver Hobert 1,6

- ¹Department of Biological Sciences, Howard Hughes Medical Institute, Columbia University, New York, NY 10027, USA
- ²Department of Physics, Center for Brain Science, Harvard University, Cambridge, MA 02138, USA
- ³Departments of Statistics and Neuroscience, Grossman Center for the Statistics of Mind, Center for Theoretical Neuroscience, Zuckerman Institute, Columbia University, New York, NY 10027, USA
- ⁴Department of Statistics and Data Science Initiative, Harvard University, Cambridge, MA 02138, USA
- ⁵Department of Physics, Northeastern University, Boston, MA 02115, USA
- ⁶Senior author
- ⁷Lead Contact
- *Correspondence: eiy1@columbia.edu https://doi.org/10.1016/j.cell.2020.12.012

SUMMARY

Comprehensively resolving neuronal identities in whole-brain images is a major challenge. We achieve this in *C. elegans* by engineering a multicolor transgene called NeuroPAL (a neuronal polychromatic atlas of landmarks). NeuroPAL worms share a stereotypical multicolor fluorescence map for the entire hermaphrodite nervous system that resolves all neuronal identities. Neurons labeled with NeuroPAL do not exhibit fluorescence in the green, cyan, or yellow emission channels, allowing the transgene to be used with numerous reporters of gene expression or neuronal dynamics. We showcase three applications that leverage NeuroPAL for nervous-system-wide neuronal identification. First, we determine the brainwide expression patterns of all metabotropic receptors for acetylcholine, GABA, and glutamate, completing a map of this communication network. Second, we uncover changes in cell fate caused by transcription factor mutations. Third, we record brainwide activity in response to attractive and repulsive chemosensory cues, characterizing multimodal coding for these stimuli.

INTRODUCTION

Whole-brain imaging and molecular profiling are widely used to study nervous system development and brain function (Ahrens and Engert, 2015; Jones et al., 2009; Lichtman and Denk, 2011; Zeng and Sanes, 2017). One limitation in interpreting whole-brain images is the difficulty of assigning unique identities to every neuron in a volume of densely packed and similarly labeled cells. Identifying neurons is a challenge even in small nervous systems like that of the nematode C. elegans. Although it is possible to perform multi-neuronal functional imaging with single-cell resolution in C. elegans (Kato et al., 2015; Kotera et al., 2016; Nguyen et al., 2016; Venkatachalam et al., 2016), identifying neurons remains laborious and uncertain, requiring substantial expertise, even in light of recent advances (Bubnis et al., 2019; Toyoshima et al., 2020). The approach of using separate and sparsely labeled landmark strains is often helpful, but not easily scalable. Many neurons lack well-established reporters, and it is not always possible to cross-validate every neuron of interest in a densely labeled volume, even with a suitable landmark strain. Moreover, although the C. elegans nervous system is widely regarded as stereotyped, this stereotypy does

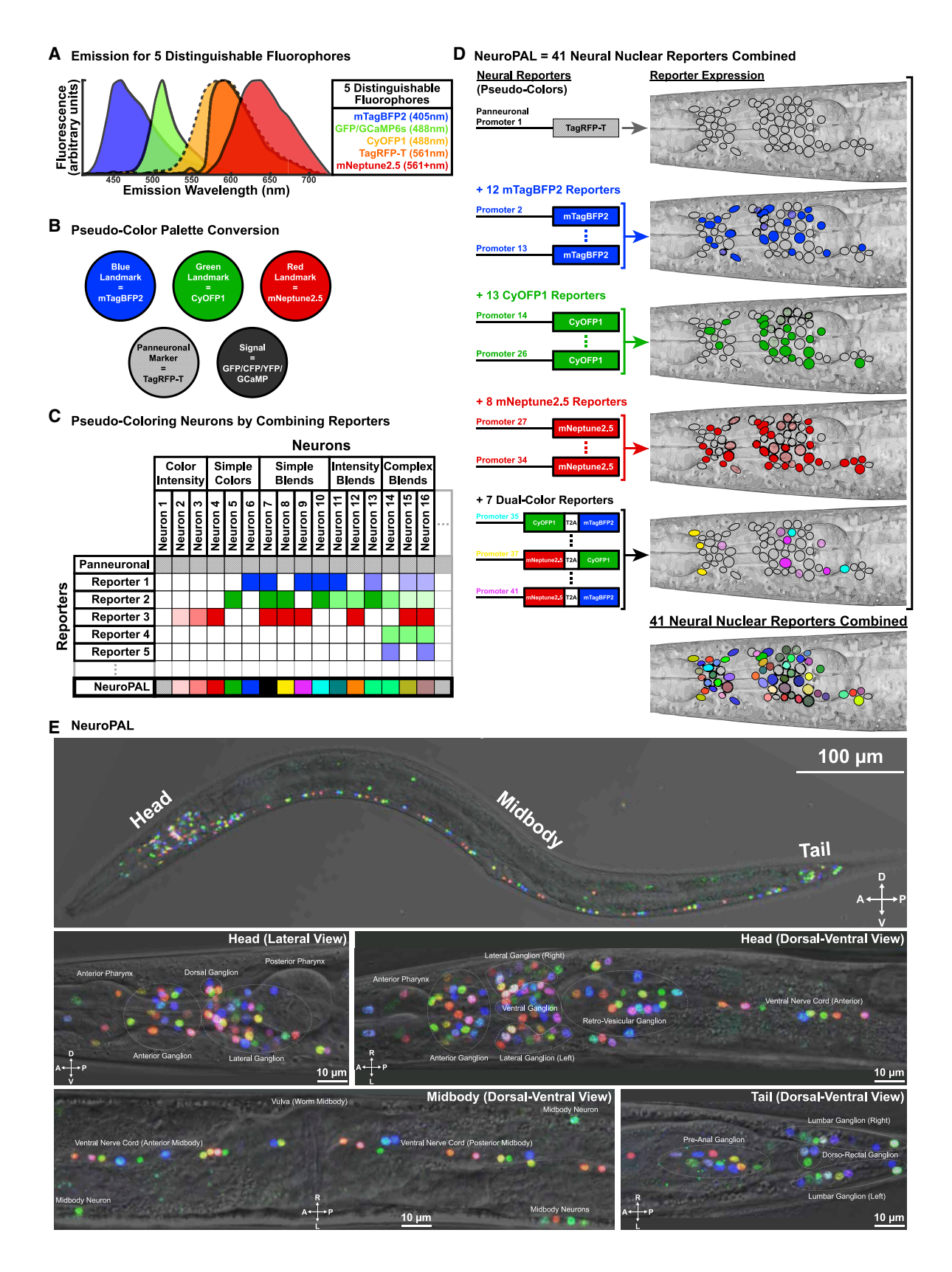
not extend to the relative positions of cell bodies within ganglia (White et al., 1986). An invariant color map of all neurons is thus needed to achieve comprehensive cell identification. Here, we leveraged the small size of the worm nervous system and its powerful genetics to develop a method that identifies all neurons in a whole-brain image with a single reagent. We describe the development of a transgene that we call NeuroPAL (a neuronal polychromatic atlas of landmarks).

The NeuroPAL transgene contains a combination of 41 selectively overlapping neuron-specific reporters, each of which expresses a subset of four distinguishably colored fluorophores. The NeuroPAL combination of reporters and colors generates a comprehensive color-coded atlas for the entire hermaphrodite nervous system. Our approach is fundamentally different from previously described "Brainbow" approaches (Livet et al., 2007; Richier and Salecker, 2015; Weissman and Pan, 2015). In "Brainbow," multicolor labeling of the nervous system occurs when each neuron randomly expresses a subset of fluorophores. In NeuroPAL, each neuron expresses a stereotyped combination of fluorophores. NeuroPAL yields an invariant color map across individuals, where every neuron is uniquely identified by its color and position. We engineered NeuroPAL to be compatible with









(legend on next page)





widely used reporters for gene expression and neuronal activity. None of the NeuroPAL fluorophores emit in the spectral bands of green, cyan, or yellow fluorescent proteins. Thus, NeuroPAL can be co-expressed with numerous markers—GFP, CFP, YFP, mNeonGreen, or reporters of neuronal dynamics like GCaMP—without affecting its color map.

We demonstrate the versatility of NeuroPAL in studies of gene expression patterns, cell fate, and whole-brain activity imaging. First, we mapped with single-neuron resolution the complete gene expression patterns of all metabotropic receptors for common neurotransmitters (acetylcholine, GABA, and glutamate) encoded in the C. elegans genome. Second, we analyzed neuronal fate defects caused by mutations in the highly conserved transcription factors (TFs) EOR-1/PLZF and PAG-3/Gfi. Third, we measured the complete whole-brain activity responses to a gustatory repellent and two olfactory attractants. To facilitate the use of NeuroPAL, we provide an open-source software package that enables semi-automated identification of all neurons in whole-brain images. To extend the NeuroPAL technique for general use, we also provide software that chooses reporter-fluorophore assignments for other tissue and organisms. In conclusion, NeuroPAL now allows the C. elegans community to easily identify all neurons in whole-brain images for diverse applications.

RESULTS

Constructing the Color Palette for Comprehensive Landmarks

The *C. elegans* nervous system contains 302 neurons (organized into 118 different classes) distributed among 11 ganglia throughout the body (Sulston, 1983; White et al., 1986). The set of neurons in each ganglion are the same from animal to animal, but the relative location of cell bodies within each ganglion is variable. The largest ganglia contain around 30 neurons. We reasoned that roughly 30 unique colors would be needed to reliably identify all neurons in each ganglion, and thus all neurons in the nervous system. Three spectrally distinct fluorophores,

distinguishable at four or more different levels (high, medium, low, and undetectable), yield at least 64 different colors. Thus, three carefully chosen fluorophores should be enough to land-mark the entire *C. elegans* nervous system (Figure 1).

We wanted our landmark reagent to be usable in animals that co-express transgenic reporters for gene expression or neuronal dynamics. The most popular fluorescent reporters include CFP, GFP/GCaMP, and YFP. We did not want our landmark fluorophores to contaminate emission signals from any of these reporters and vice-versa. Therefore, we sought fluorophores with unique excitation/emission profiles that also left free the cyan, green, and yellow emission bands. We tested a wide variety of fluorophores and found mTagBFP2, CyOFP1, mNeptune2.5, and TagRFP-T to be the best available candidates (Figure 1A; STAR Methods; Chu et al., 2014, 2016; Shaner et al., 2008; Subach et al., 2011). By pseudo-coloring these fluorophores blue, green, red, and white, respectively, their combinations generate RGB pseudo-colors (Figures 1B and 1C).

Given the resolution limitations of light microscopy, we did not want fluorescence signals from neighboring cells to contaminate one another. To minimize spatial overlap in fluorescence emission, we localized fluorophore expression to cell nuclei via nuclear-localization sequences or histone tagging. We assigned one fluorophore, TagRFP-T, to act as a panneuronal label. To minimize differential and variable expression levels associated with many known panneuronal drivers (Stefanakis et al., 2015), we constructed a synthetic ultra-panneuronal (UPN) driver by fusing the *cis*-regulatory elements of four different panneuronally expressed genes (Table S1). The UPN driver delivered bright, nearly uniform expression of TagRFP-T throughout the nervous system.

Empirical Assembly of NeuroPAL, a Transgene Combining Neuronal Landmarks

Next, we sought to differentially express the remaining three fluorophores (mTagBFP2, CyOFP1, and mNeptune2.5) to enable unique neuronal identification (Figures 1C and 1D). We used two criteria to build a stereotyped cellular color map for

Figure 1. NeuroPAL Method and Images

(A) The emission for five distinguishable fluorophores. Each fluorophore's excitation wavelength is listed in parentheses.

(B) Fluorophores are converted into pseudo colors to construct a primary color palette. Three fluorophores are designated as landmarks and pseudo colored to construct an RGB color palette: mNeptune2.5 is pseudo-colored red, CyOFP1 is pseudo-colored green, and mTagBFP2 is pseudo-colored blue. The fluorophore TagRFP-T is used as a panneuronal marker. The fluorophores GFP/CFP/YFP/GCaMP are reserved for reporters of gene expression or neuronal activity. TagRFP-T and GFP/CFP/YFP/GCaMP are visualized separately from the RGB landmarks to avoid confusion. They can be assigned any pseudo color.

(C) An example of how to stably pseudo color neurons, across animals. A set of reporters (rows), with stable neuronal expression (columns), are used to drive the fluorophores (table elements). NeuroPAL colors (last row) result from the combined patterns of reporter-fluorophore expression. The panneuronal reporter is expressed in all neurons. The remaining reporters have differential neuronal expression patterns and are used to drive the pseudo-colored landmark fluorophores. Combinations of these differentially expressed reporters assign stable and distinguishable pseudo colors to neurons. For example, reporter 3 drives the red landmark fluorophore (mNeptune2.5), to color neurons 2–4 with distinguishable red intensities and contributes to the blended coloring of several other neurons. In contrast, neuron 1 does not express any of the landmark fluorophores but is still marked by the panneuronal reporter.

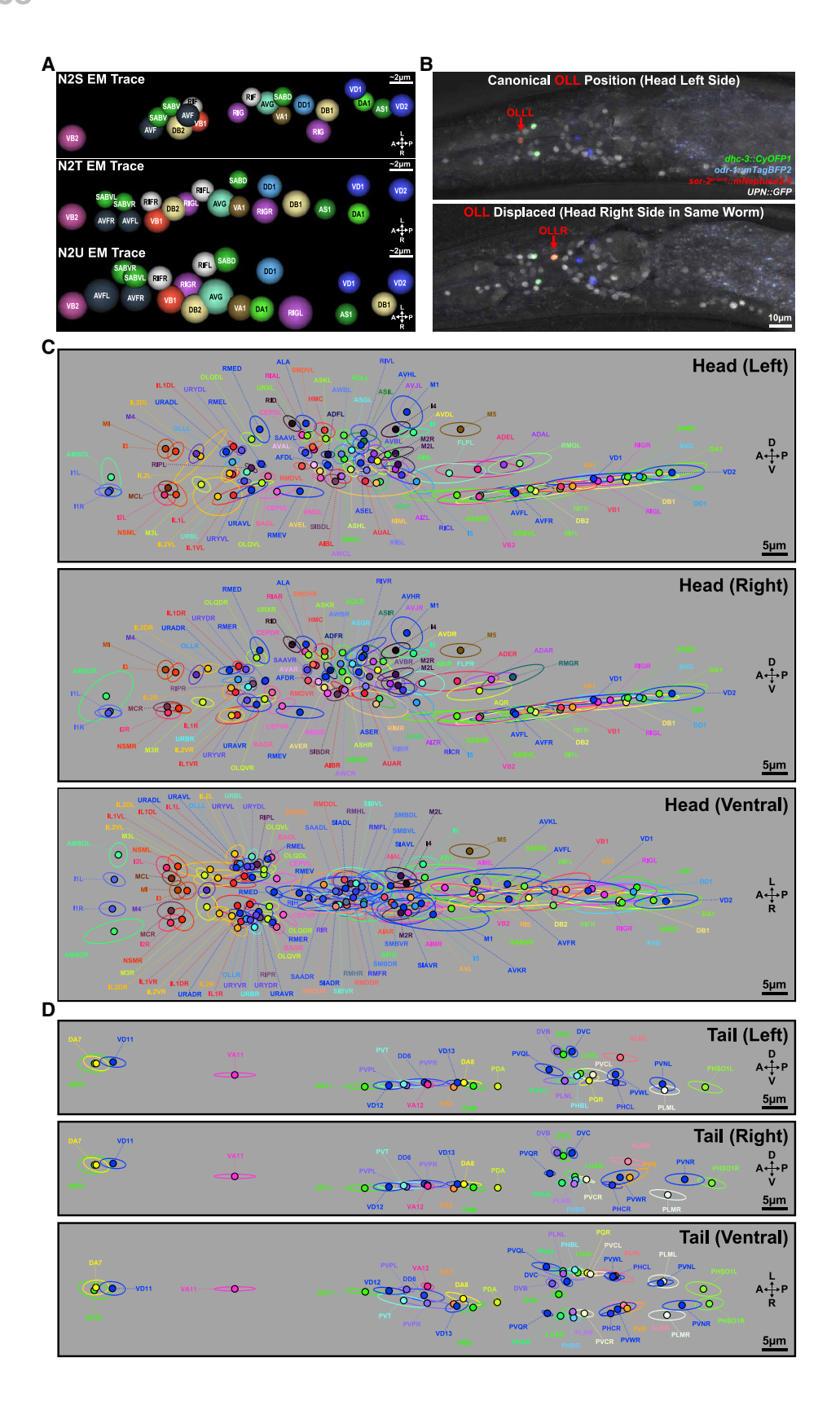
(D) NeuroPAL scales this concept to 41 reporters that, in combination, disambiguate every neuron in *C. elegans* and thus generate, a single stereotyped color map across all animals (see Table S1 for data). Seven of the NeuroPAL reporters use a self-cleaving peptide sequence (T2A) to simultaneously drive expression of two different colors.

(E) Young adult NeuroPAL worms have a deterministic color map that remains identical across all animals (see Videos S1 and S2 for 3D images). Each neuron is distinguishable from its neighbors via color. All worm ganglia are shown.

All images may employ histogram adjustments to improve visibility. Images without a transmitted light channel (e.g., Nomarski) may further be adjusted with a gamma of \sim 0.5 to improve visibility on the dark background.

See also Table S1 and Videos S1 and S2.

See Figures S1 and Table S2 for phenotypic analysis.



(legend on next page)





unambiguous and comprehensive assignment of identity: (1) each neuron should express a stable amount of each fluorophore, across animals; and (2) nearby neurons in each ganglion should express visually distinguishable amounts of the fluorophores.

We began with a candidate list of 133 published neuronal reporters known to have differential gene expression patterns. This list included both broad and narrowly expressed reporters (Table S1). We validated and completed identification of the expression of these candidates by co-expressing them with well-characterized cell-identity reporters. Candidates with variable or weak expression were dropped from further consideration. We then proceeded empirically and iteratively to build a single transgene for comprehensive neuronal identification. We started with a small set of broadly expressed reporters that spanned most of the nervous system. We gradually expanded this initial set, adding and changing reporters so as to target progressively smaller subsets of neurons that needed distinguishable colors. In each iteration, we assessed which neurons could and could not be identified based on color and position. We repeated these steps by trial and error until we found a suitable transgene that colored all neurons distinguishably from every neighboring cell. The final transgene, composed of 41 different reporter-fluorophore fusions, allowed us to unambiguously assign identities to every neuron in C. elegans based on a stereotyped color map (Figure 1E; Table S1; Videos S1 and S2; Neuro-PAL manuals: https://www.hobertlab.org/neuropal/). We called this transgene NeuroPAL.

Neuronal Color Verification and Phenotypic Assessment of NeuroPAL Strains

We integrated the extrachromosomal NeuroPAL transgene into the genome, outcrossed the brightest integrants (otls669, otls670, and otls696) eight times, and confirmed that these transgenes exhibited stable expression for more than 100 generations. The color scheme of the NeuroPAL strains mostly matched our expectations based on the combination of reporter-fluorophore fusions used in their construction. We verified the identity of each neuron by crossing the NeuroPAL integrants to 25 different GFP reporter lines with well-defined expression patterns (Table S1). The position, color, and identity of all neurons were verified using predominantly two or more GFP reporter lines and multiple NeuroPAL integrants. We found that the NeuroPAL expression pattern was stable, robust, and stereotyped throughout the nervous system over hundreds of scored animals (see NeuroPAL manuals: https://www.

hobertlab.org/neuropal/). A minor exception was four neuron classes that exhibited variable brightness (AVL, RIM, RIS, and PVW). This minor variability did not affect our ability to comprehensively identify all neurons.

We assessed the general health of our NeuroPAL integrants (Figures S1A–S1G; Table S2). All NeuroPAL integrants were able to be revived from frozen stock and generate progeny from either hermaphrodite or male parents. Thus, every integrant can be combined with other transgenic reporter lines using genetic crosses. We tested all NeuroPAL integrants with standard assays including brood size, growth, morphology, locomotion, and chemotaxis. The brightest integrant was otls669 (strain OH15262). The integrant with locomotion and chemotactic behavior closest to wild-type, otls670 (strain OH15263), is less bright but perhaps more suitable for behavioral analysis and calcium imaging. All NeuroPAL integrants are available at the Caenorhabditis Genetics Center (CGC).

Variability in Neuronal Cell Body Positions

The C. elegans hermaphrodite nervous system is widely regarded as stereotyped. However, the original electron-micrograph reconstructions (White et al., 1986) and subsequent analysis (Toyoshima et al., 2020) have reported variability in the positions of individual cell bodies within each ganglion of the nervous system. Variability in the position of individual cell bodies makes it impossible to assign neuronal identities based on relative position alone (Figures 2A and 2B), underscoring the need for a reagent like NeuroPAL that disambiguates these identities based on genetic-expression factors. Nevertheless, a probabilistic map of neuronal positions would be useful in many studies. To construct this probabilistic map, we globally aligned neurons in the head and tail of 10 young-adult NeuroPAL hermaphrodites (otls669) of identical age and measured the spatial coordinates of every neuron (Table S3; Methods S1). This map revealed different positional variability across neuron types (Figures 2C and 2D).

Expression Maps for All Metabotropic Neurotransmitter Receptors

To showcase NeuroPAL as a tool for expression-pattern analysis, we focused on neurotransmitter-signaling maps. Maps of neurotransmitter expression have been determined for the entire *C. elegans* nervous system (Gendrel et al., 2016; Pereira et al., 2015; Serrano-Saiz et al., 2013). Postsynaptic neurons receive neurotransmitter signals by either ionotropic or metabotropic receptors. However, the map of neurotransmitter receptor

Figure 2. Neuron Locations and Their Positional Variability

(A) Neuron locations and variability, in the retrovesicular ganglion, taken from electron micrographs of three adult hermaphrodites N2S, N2T, and N2U (Hall and Altun, 2007; White et al., 1986).

(B) An example of substantial positional variability. The OLL left (OLLL) and right (OLLR) neurons, within a single animal, should share equivalent positions. Instead they show substantial anterior-posterior displacement relative to each other. The transgenic reporters and their pseudo colors are noted on the figure. (C and D) Canonical neuron locations (filled circles displaying the NeuroPAL colors) and their positional variability (encircling ellipses with matching colors) for all ganglia, as determined by NeuroPAL (otls669, strain OH15262) (see Table S3 for data). Positional variability is shown as the 50% contour for neuronal location (measured as a Gaussian density distribution), sliced within a 2D plane (Methods S1). We show both the left-right and dorsal-ventral planes to provide a 3D estimation of positional variability. (C) Left, right, and ventral views of the head neuron positions. OLLR exhibits over twice the positional variability of OLLL in its anterior-posterior axis, echoing the displacement seen with the non-NeuroPAL transgene in (B). (D) Left, right, and ventral views of the tail neuron positions. See also Table S3 and Methods S1.



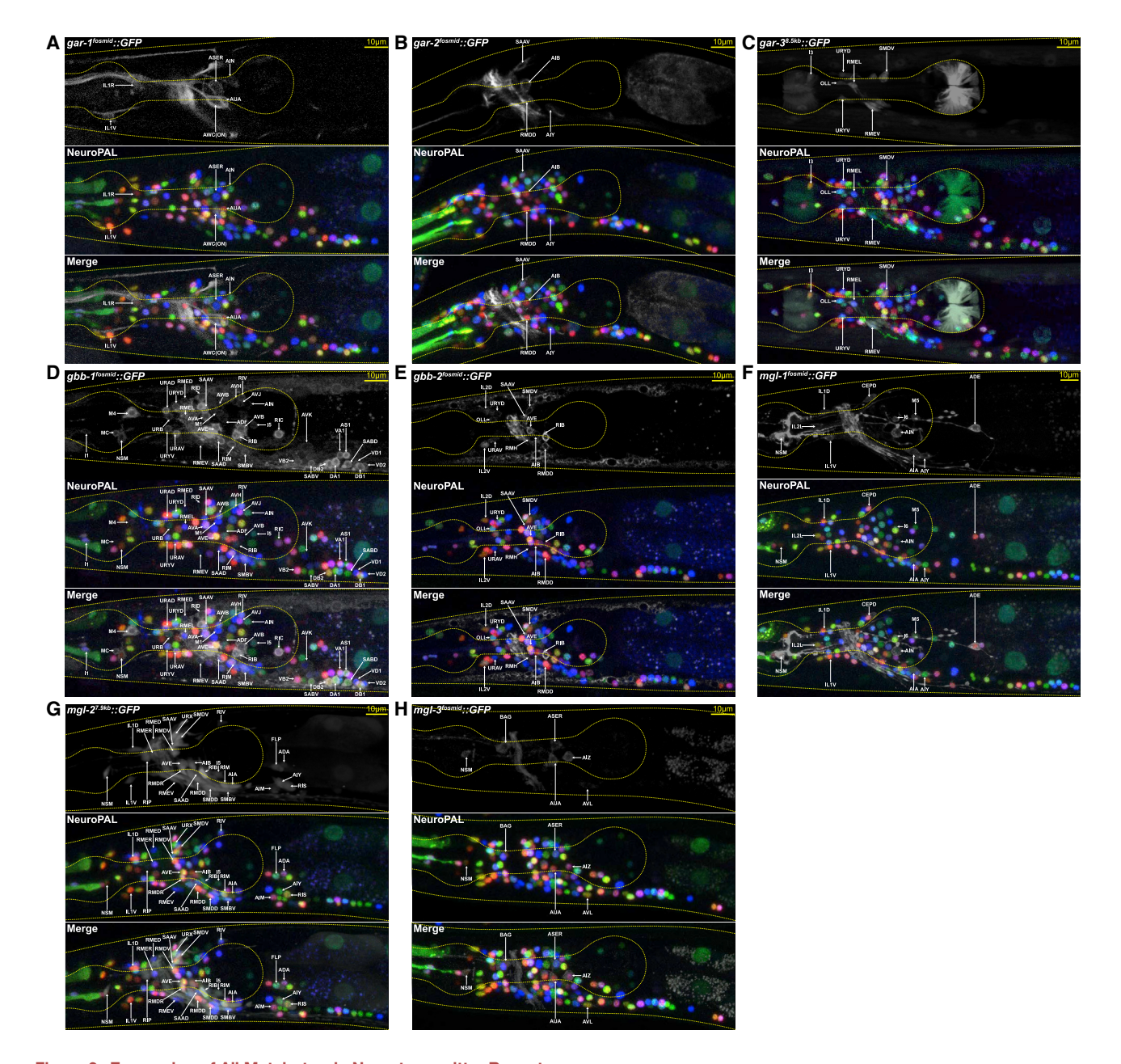


Figure 3. Expression of All Metabotropic Neurotransmitter Receptors

(A-H) NeuroPAL is used to identify the GFP expression patterns for all metabotropic neurotransmitter receptors (Table S4): the three acetylcholine receptors (A) GAR-1, (B) GAR-2, and (C) GAR-3; the two GABA receptors (D) GBB-1 and (E) GBB-2; and the three glutamate receptors (F) MGL-1, (G) MGL-2, and (H) MGL-3. See also Table S4.

expression remains largely unknown, leaving their communication networks incomplete. We used NeuroPAL to map the complete expression of all metabotropic neurotransmitter receptors. The worm genome predicts three cholinergic metabotropic receptors (gar-1, gar-2, and gar-3), three glutamatergic metabotropic receptors (mgl-1, mgl-2, and mgl-3), and two GABAergic metabotropic receptors (gbb-1 and gbb-2) (Hobert, 2013; Figures 3 and 4A). Crossing primarily fosmid-based gfp reporter transgenes into a NeuroPAL background, we find that these receptors are expressed in 97% of all neurons: 70% express GARs, 54% express MGLs, and 89% express GBBs (Figure 4C; Table S4). Previous work identified all presynaptic GABAergic neurons as well as all postsynaptic ionotropic GABAA receptor-expressing neurons (Bamber et al., 1999; Beg and Jorgensen, 2003; Gendrel et al., 2016; Jobson et al., 2015). Thus, our GBB map (the identity of every GABA_B receptor-expressing neuron) has completed the GABA communication network in C. elegans (Figure 4B).



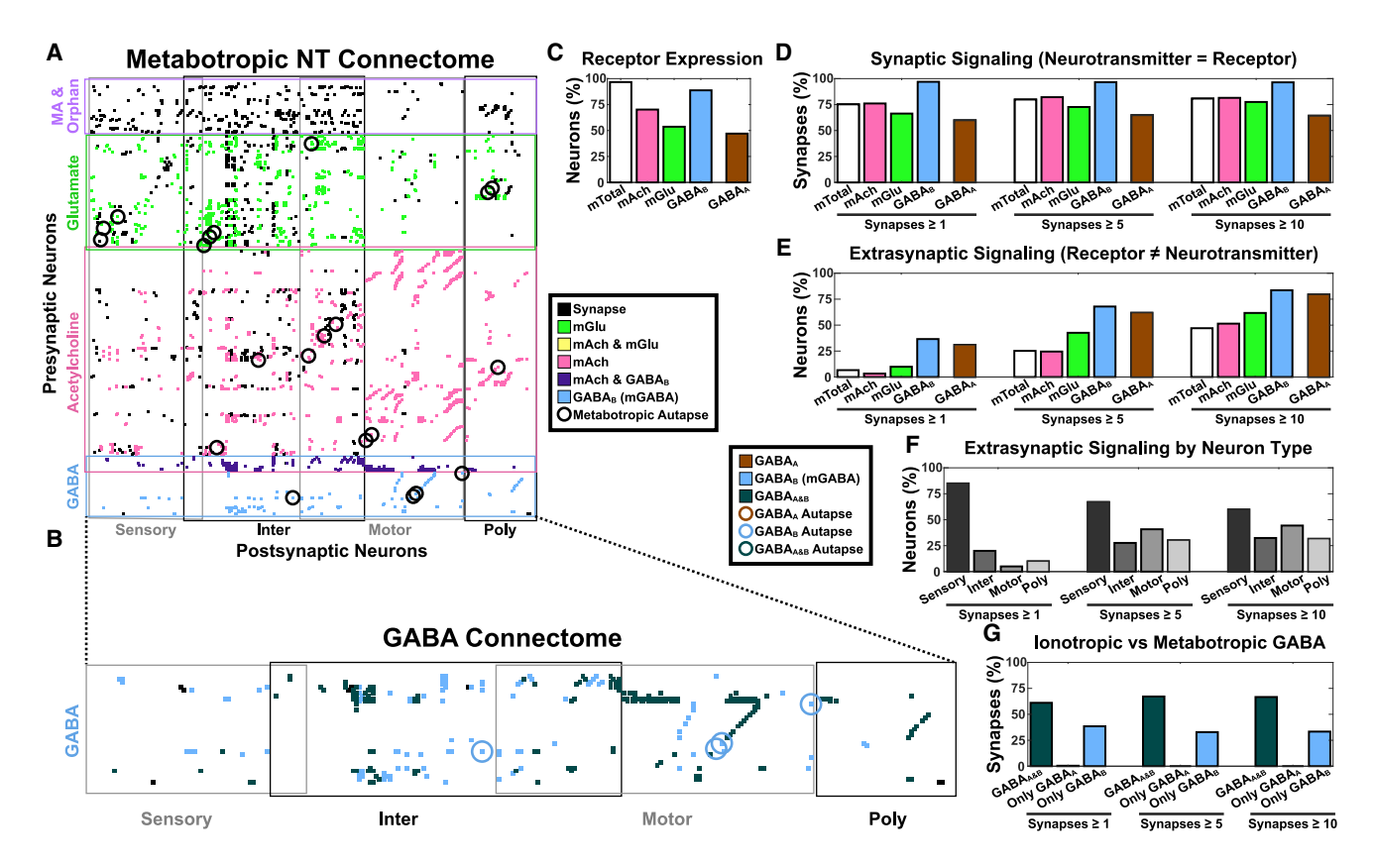


Figure 4. Metabotropic Neurotransmitter Communication Network

(A) Expression of the metabotropic neurotransmitter receptors incorporated into the existing, anatomically defined connectome. Rows are presynaptic neurons (organized by neurotransmitter). Columns are postsynaptic neurons (organized by neuron type). Cognate synaptic connections (where the presynaptic neurotransmitter matches the postsynaptic metabotropic receptor) are marked by a colored dot (see legend for neurotransmitter coloring). All other synaptic connections are marked by a black dot. Metabotropic autapses with cognate self-connectivity are circled.

- (B) The complete GABA communication network: all presynaptic GABA neurons and their corresponding postsynaptic ionotropic GABA_A and metabotropic GABA_B expressing neurons. Synaptic connections are marked by a colored dot to indicate postsynaptic GABA_A and/or GABA_B receptors (see legend for receptor-type coloring). GABA autapses are circled. All GABAergic autapses express $GABA_B$ receptors and none express $GABA_A$ receptors.
- (C) Metabotropic (and ionotropic GABA_A) receptor expression as a percentage of all neurons. Metabotropic receptors are expressed in almost all neurons.
- (D) Synaptic connections with cognate neurotransmitter receptors as a percentage of the total synapses associated with each neurotransmitter. Metabotropic communication is extensive and these percentages are robust when removing weak synaptic connections by thresholding for at least 1, 5, or 10 synapses. A polyadic synapse that connects AVF (a neuron with no means of releasing its GABA) onto AIM and several cognate GABA_B expressing neurons, reduces our count of GABA synaptic signaling to just under 100%.
- (E) Neurons expressing a neurotransmitter receptor that have no presynaptic partners expressing their cognate neurotransmitter. The absence of presynaptic GABAergic partners for over 31% of the GABA_A and 37% of the GABA_B receptor-expressing neurons suggests substantial extrasynaptic GABA signaling. For each neurotransmitter, we show the percentage of neurons lacking a cognate presynaptic partner relative to all neurons expressing the neurotransmitter receptor. Removing weak synaptic connections increases the potential for extrasynaptic signaling.
- (F) The types of neurons expressing a neurotransmitter receptor that have no presynaptic partners expressing their cognate neurotransmitter (suggesting extrasynaptic signaling). We show the neuron type percentages. Sensory neurons represent the majority and are robust against removing weak synaptic connections. Neurons are often categorized as multiple types and thus the sum of percentages can exceed 100%.
- (G) Ionotropic versus metabotropic GABA communication. Over 60% of GABA connections share both GABA_A and GABA_B receptors at their postsynaptic sites. The remaining nearly 40% of connections are accounted for solely by metabotropic GABAB at the postsynaptic sites. These percentages remain robust when removing weak synaptic connections.

Metabotropic receptor abbreviations: acetylcholine, mAch; glutamate, mGlu; GABA, GABA_B; all, mTotal. The ionotropic GABA receptor is abbreviated GABA_A. See Table S4 for data.

We compared the GABA communication network to the synaptic connectivity between all cells as predicted by the recently updated C. elegans wiring diagram (Figures 4B and 4G; Cook et al., 2019). We found that every postsynaptic partner of every GABA-releasing neuron expresses one of the two GABA_B receptors. In contrast, only 60% of postsynaptic partners of GABAergic neurons express any of the seven GABAA receptors (Gendrel et al., 2016). Metabotropic communication similarly extends broadly over the cholinergic and glutamatergic signaling networks: 76% of the postsynaptic partners of cholinergic





neurons express GAR receptors, and 66% of the postsynaptic partners of glutamatergic neurons express MGL receptors (Figure 4D).

Surprisingly, we found that a considerable portion of the neurons expressing GABA receptors do not receive any connections from a presynaptic GABAergic neuron (Figure 4E); 31% of GABA_A and 37% of GABA_B receptor-expressing neurons have no presynaptic GABAergic partner. Moreover, we found 92% of all neurons express GABA receptors, and yet only 10% of neurons release GABA. These results suggest widespread extrasynaptic GABA communication. Such extrasynaptic communication may also be present for the other metabotropic neurotransmitter receptors: 3% of neurons that express GAR receptors and 10% of neurons that express MGL receptors do not receive synaptic inputs from any glutamatergic and cholinergic neurons, respectively (Figure 4E). Notably, sensory neurons appear to be the most prominent recipients of extrasynaptic communication (Figure 4F).

Uncovering Determinants of Cell Fate

The 41 reporters used to assemble NeuroPAL each serve as indicators of neuronal differentiation and identity. Thus, mutations that affect cell fate can cause informative changes in the Neuro-PAL color map as different neuron types acquire different genetic identities. Therefore, NeuroPAL provides a fast method to screen for multiple cell-fate alterations. As an example, the conserved TF PAG-3/Gfi has been shown to orchestrate the fates of the VA and VB ventral motor neuron classes (Cameron et al., 2002). We crossed NeuroPAL (otls669) with strains carrying null alleles of pag-3 (n3098 and ok488). As predicted, the color codes that identify the VA and VB cell types in NeuroPAL are absent in pag-3 mutants (Figures 5A and 5B; Table S5). Unexpectedly, we also found color changes in the AVE and PVR interneurons caused by pag-3 mutation. By checking a fosmid-based reporter, we discovered pag-3 expression in neurons that had gone previously unidentified, including AVE and PVR (Figure 5C; Table S5).

NeuroPAL is particularly useful when the expression pattern of presumptive cell fate regulators is either unknown or too broad to easily formulate hypotheses about their effects on cell identity. As an example, we examined EOR-1/PLZF, a ubiquitously expressed and highly conserved TF (Howard and Sundaram, 2002). Given its ubiquitous expression (Figure 5D), EOR-1 may be involved in controlling the differentiation program of anywhere between none to all of the worm's neurons. By crossing eor-1 null mutants (cs28 and ok1127) to NeuroPAL, we discovered neuron-subtype-specific differentiation defects. The dorsal and ventral RME neurons (RMED/V) lost all their blue coloring but retained their panneuronal label (Figures 5E and 5F; Table S5). In contrast, the left and right RME neurons (RMEL/R) exhibited no changes in their color codes. Expression of the blue landmark fluorophore in the RME neurons is driven by three reporters: ggr-3, pdfr-1, and unc-25/GAD (Table S1). We validated the NeuroPAL color alterations with an endogenously tagged reporter allele of unc-25/GAD (Figures 5E and 5G; Table S5), but at the same time found no defects in UNC-47/VGAT expression. In conclusion we have identified a selective function of the ubiquitously expressed EOR-1 protein in the RME neuron class, a function that would have been impossible to predict based on the ubiquitous expression of EOR-1.

Whole-Brain Activity Imaging of Gustatory and Olfactory Responses

A major challenge in analyzing panneuronal calcium imaging data in C. elegans has been determining neuronal identities (Kato et al., 2015; Nguyen et al., 2016; Venkatachalam et al., 2016). To solve this problem, we combined NeuroPAL with the panneuronally expressed calcium reporter GCaMP6s (strain OH16230). We then used multicolor imaging to comprehensively identify all neurons. We recorded 21 worm heads (189 neurons) and, separately, 21 worm tails (42 neurons), with a median representation of 18 animals per neuron type. We studied brainwide responses, in young-adult hermaphrodites, to a repulsive taste (160 mM NaCl) and two attractive odors (10⁻⁴ 2-butanone and 10^{-4} 2,3-pentanedione), each previously described to activate different sensory neurons (Bargmann et al., 1993; Bargmann and Horvitz, 1991; Ward, 1973; Wes and Bargmann, 2001). These stimuli were delivered in chemotaxis buffer to the nose of the animal using a multichannel microfluidic device (Figures 6A and 6B; Table S6; Videos S3 and S4; STAR Methods; Si et al., 2019). We subjected each animal to the three chemical stimuli delivered in a randomized order (10-s pulses spaced by 50-s intervals). Using activity traces from all identified neurons, we assembled the mean brainwide response to each stimulus. Brainwide imaging revealed both known and previously unknown neuronal responses to each stimulus, encompassing multiple sensory and interneurons, many of which were not previously implicated in behavioral responses (Figure 6C). Additionally, we imaged another strain OH15500 (otls669;otls672), self-crossed 23× to drive isogenicity (Table S6), wherein we used a higher concentration and duration of NaCl (200 mM for 20 s) and delivered stimuli in water instead of buffer. OH15500 results are available in the supplement and not discussed further herein.

As previously reported (Ortiz et al., 2009; Pierce-Shimomura et al., 2001; Suzuki et al., 2008; Thiele et al., 2009), NaCl evoked stereotyped left/right (L/R) asymmetric responses in the two ASE neurons. However, ASER exhibited an increase in [Ca²⁺] upon NaCl presentation, a result that likely reflects our choice of a much higher repulsive NaCl concentration, compared to previously published experiments (Ortiz et al., 2009; Suzuki et al., 2008). We observed many responses in a large number of sensory and interneurons, corresponding to the NaCl stimulus pulse (Figures 6C-6F; Table S6). In particular, we detected significant NaCl responses in six interneurons with no previously known function: AIN, AVF, AVH, AVJ, I2, and MI.

We found that odors also evoked responses in a large set of both sensory and interneurons, throughout the brain, but exhibited more inhibitory activity (decreasing [Ca2+]) than seen for NaCl (Figure 6C). As in previous work (Wes and Bargmann, 2001), 2-butanone and 2,3-pentanedione evoked stochastically asymmetric responses in the AWCON/OFF neuron pair (Figure 6D); srsx-3 distinguishably colors AWCOFF in NeuroPAL (Bauer Huang et al., 2007). The set of neurons activated by all three stimuli was partly overlapping but distinct for each stimulus (Figures 6C-6F). For example, the ASJ sensory neurons



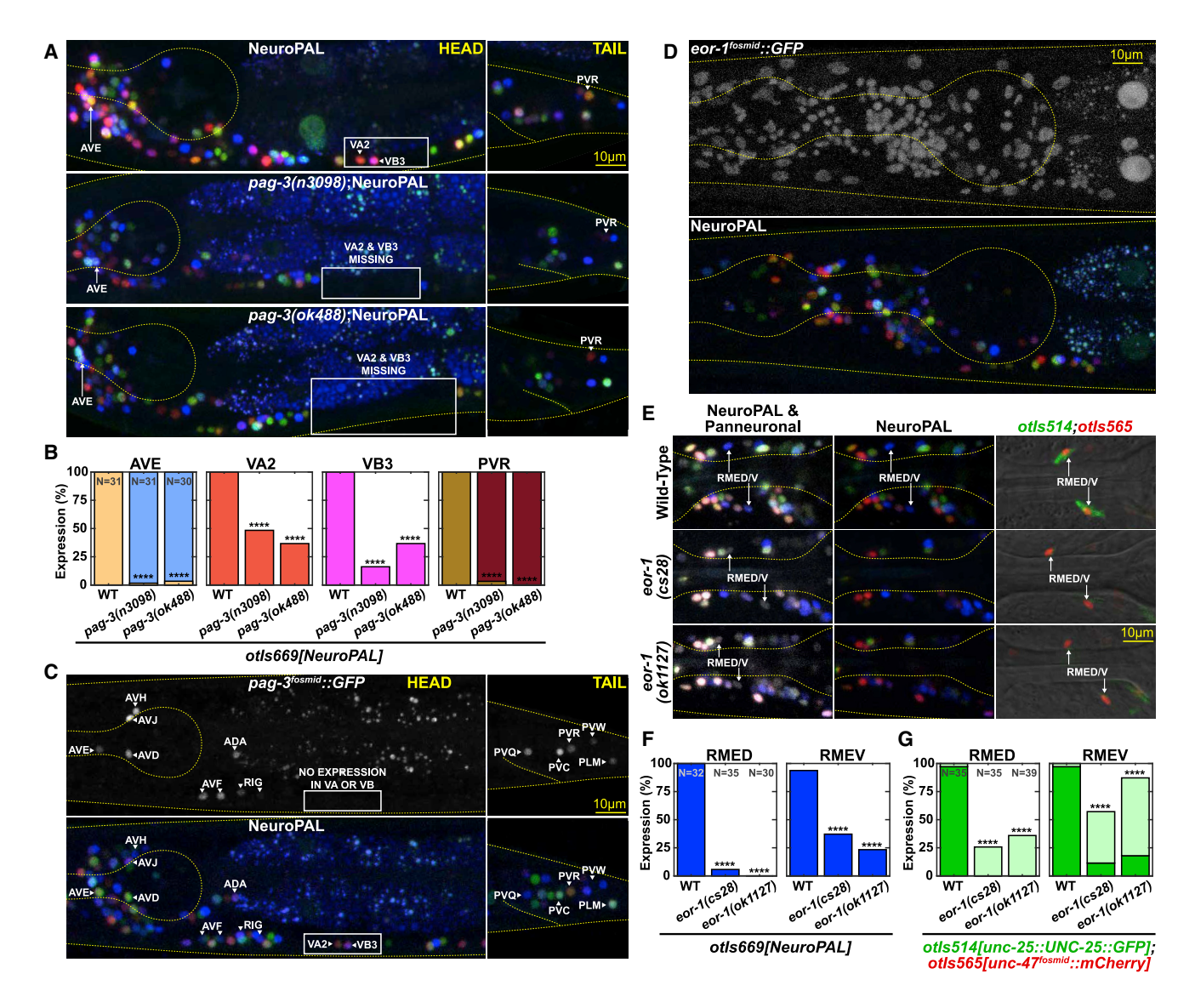


Figure 5. Mutant Analysis of the Conserved Transcription Factors PAG-3/Gli and EOR-1/PLZF

(A and B) Alterations in NeuroPAL coloring reveal neurons with altered fate in pag-3(-) mutant backgrounds: the AVE pre-motor interneuron gains blue-color expression, the PVR interneuron loses all green-color expression, and the VA and VB motor neurons are missing entirely. Statistical bar graph colors in (B) are sampled from the images in (A).

(C) PAG-3/Gli expression as assessed with a fosmid reporter (wgls154): ADA*, ALM, AQR*, AVD*, AVE*, AVF, AVH*, AVJ*, AVM, BDU, DVC*, I1*, I2*, I6*, PLM, PQR*, PVC*, PVM, PVQ*, PVR*, PVW*, RID*, RIG, RMG*, VA11-12, and URY* (*previously unpublished expression).

(D) EOR-1/PLZF has broad, likely ubiquitous, expression, as assessed with a fosmid reporter (wg/s81).

(E-G) The NeuroPAL blue reporters in RMED/V are ggr-3, pdfr-1, and unc-25.

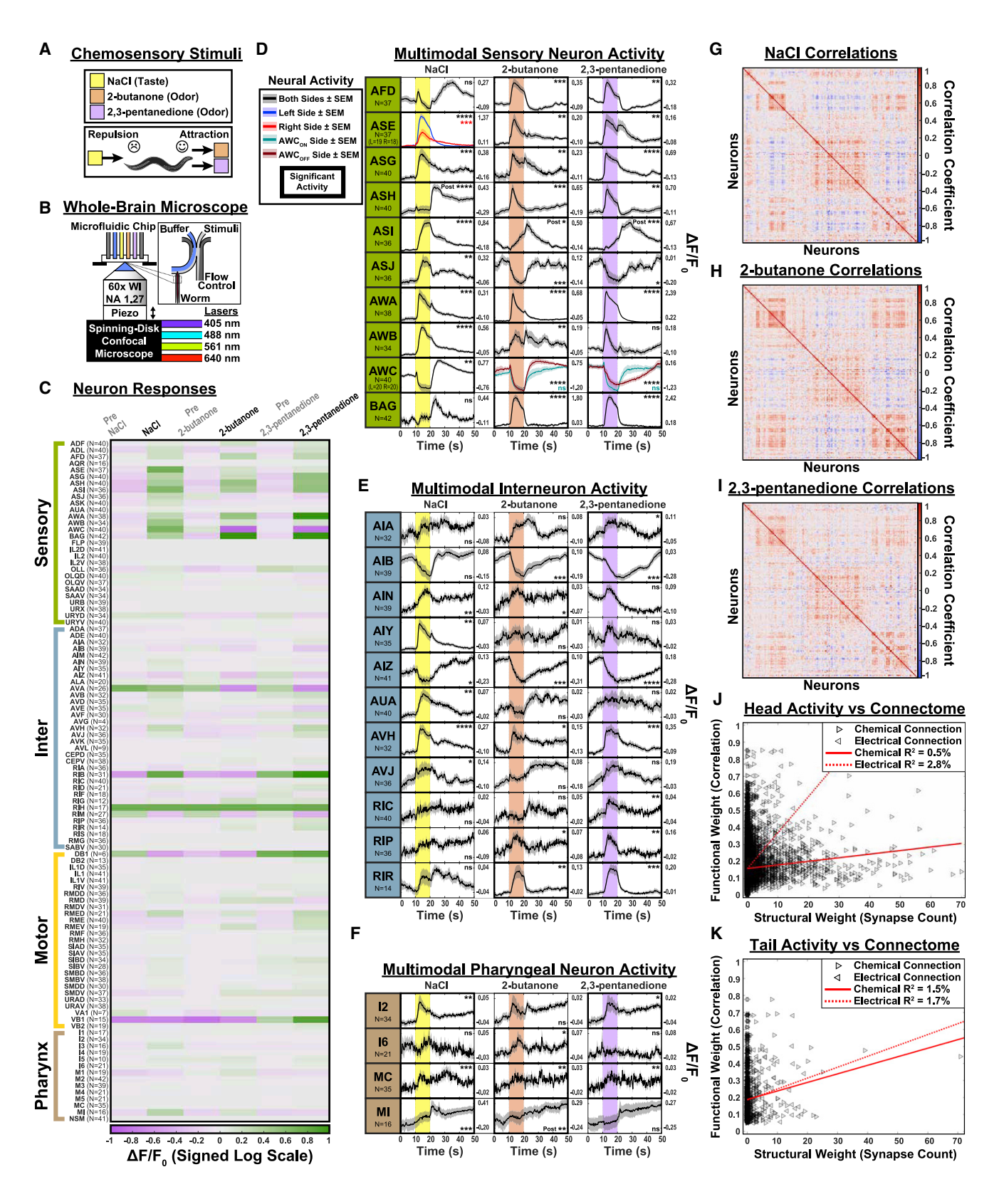
(E and F) NeuroPAL exhibits total loss of its RMED/V blue-color expression in eor-1(-) mutant backgrounds but retains panneuronal marker expression (shown in white), indicating the preservation of RMED/V neuronal fate.

(G) RMED/V fate analysis in eor-1(-) mutants with unc-25 (otls514) and unc-47 (otls565) reporter transgenes. See Table S5 for data.

were excited by NaCl but inhibited by both odors, whereas the RIC interneurons were excited solely by 2,3-pentanedione. Downstream of sensory neurons, we observed significant responses in many interneurons, many with no previously known function (e.g., AIN, AVH, RIF, RIG, and RIR) (Figures 6E and 6F; Table S6). In the tail, the PVQ interneurons were significantly excited upon presentation of 2,3-pentanedione, while a mix of sensory and interneurons exhibited significant post-stimulus responses (upon removal of the stimulus from the animal's nose) to all three stimuli (Table S6). Many of these post-stimulus responses were observed in interneurons with no previously known behavioral function (LUA, PVN, PVQ, PVR, and PVW).

Surprisingly, both salt and odors elicited responses across the pharyngeal nervous system (Figure 6F; Table S6), a heavily





(legend on next page)





interconnected network of 20 neurons that synapses with the main nervous system through a single interneuron, RIP (Cook et al., 2019). Recent anatomical re-analysis of the pharyngeal connectome revealed that most neurons in the pharynx have potential sensory endings (Cook et al., 2020). Thus, our activity recordings suggest that, despite its small size, the worm's pharyngeal network may encode its own representation of behavioral responses to chemosensory cues.

We noted that in many animals, the pair of AVF interneurons displayed robust cyclical activity for the entire 4-min recording, irrespective of delivery of gustatory or olfactory stimuli. The frequency of this activity was ~0.3 Hz, similar to the crawling frequency of freely moving worms of this strain (Figures S1G and S1H; Table S2). Previous experiments indicated that neurons in the region of the retrovesicular ganglion (the location of the AVF neurons) likely contribute to the central pattern generator for forward locomotion (Fouad et al., 2018). AVF ablation has also been shown to abolish forward locomotion (Hardaker et al., 2001). These results suggest that AVF may be part of the central pattern generator for forward locomotion in C. elegans. Further experiments will be required to confirm this hypothesis.

Whole-Brain Neuronal Dynamics and Connectivity

Exploring network-level dynamics, we computed pairwise correlations between the activities of all identified neurons, in each animal, from our whole-brain activity recordings. We found similar stimulus-specific neuronal correlations across individuals, but each stimulus generated its own brainwide correlation pattern (Figures 6G-6I and S2C-S2E). Even the two attractive odors produced distinct sets of neuronal correlations among and between sensory and interneurons. These results can be seen in the brainwide neuronal trajectories through low-dimensional PCA-space (Figures S2A and S2B). For instance, the AWB sensory neurons and their synaptically connected interneuron partners AUA and AVH exhibit distinct pairwise correlations depending on the stimulus (Figures 6D and 6E). Thus we find that brain dynamics are stimulus-specific.

We asked whether a simple relationship exists between these functional correlations and the synaptic counts previously measured from the anatomical connectome (Cook et al., 2019; White et al., 1986). To do so, we compared our correlation matrices of pairwise functional activity to the connectome matrix of pairwise synaptic connectivity. These matrices represent functional and structural measures of neuronal communication, respectively. We used the absolute value of the correlation matrices, because the connectome lacks excitatory/inhibitory synaptic information. We found low Pearson correlation between these functional and structural matrices. For electrical connectivity, $R^2 = 2.8\%$ in the head and $R^2 = 1.7\%$ in the tail, and for chemical connectivity, $R^2 = 0.5\%$ in the head and $R^2 = 1.5\%$ in the tail (Figures 6J and 6K). We tried multiple variations in our calculations (e.g., thresholding for low sampling, using ranked correlation metrics, log-scaling synaptic counts, and limiting functional activity to only stimulus or non-stimulus delivery periods) but these did not noticeably improve correlation between functional activity and the structural connectome (Table S6). The low correlation values we measured may intimate contributions from non-synaptic signaling networks (that are not reflected in the anatomical connectome). These non-synaptic signaling networks include: (1) pervasive neuropeptidergic signaling (Bargmann and Marder, 2013), (2) extensive aminergic signaling (Bentley et al., 2016), and (3) potential extrasynaptic signaling as hinted by our expression maps of the metabotropic neurotransmitter receptors (see Expression Maps for All Metabotropic Neurotransmitter Receptors).

Semi-automated Neuronal Identification

We developed an instruction guide to help researchers use Neuro-PAL (NeuroPAL manuals: https://www.hobertlab.org/neuropal/). This guide covers a variety of NeuroPAL-compatible microscope configurations and provides instructions on how to identify all neurons using the NeuroPAL color map. However, manual annotation of neurons is laborious and time-consuming. To speed annotation, we developed a software pipeline that partially automates this task (Methods S1; NeuroPAL ID software: https://www. hobertlab.org/neuropal/). This software pipeline uses three unsupervised algorithmic steps to automatically annotate neuronal identities in NeuroPAL images (Figure 7A). First, we filter out

Figure 6. Whole-Brain Neuronal Activity Imaging of Taste and Odor Responses

(A) C. elegans were subjected to three chemosensory stimuli: a repulsive taste (160 mM NaCl) and two attractive odors (10⁻⁴ 2-butanone and 10⁻⁴ 2,3pentanedione).

(B) Animals were immobilized inside a microfluidic chip. Stimuli were delivered in chemotaxis buffer. Each animal was imaged using a spinning disk confocal microscope with four excitation lasers. The NeuroPAL color map was imaged to identify all neurons. Thereafter, brainwide activity was recorded via the panneuronal calcium sensor GCaMP6s (Videos S3 and S4).

(C) Peak neuronal activity, before and during stimulus presentation, for 109 head neuron classes and subclasses.

(D-F) Neuronal activity traces for selected (D) sensory neurons, (E) interneurons, and (F) pharyngeal neurons that responded to stimuli. The 10-s stimulus delivery period is indicated by the vertical colored bar. Black activity traces represent all neurons combined into one representative group. Colored activity traces divide neurons into groups exhibiting known asymmetric responses: stereotyped asymmetries between the ASEL and ASER neuron pair and stochastic asymmetries between the \bar{AWC}^{ON} and \bar{AWC}^{OFF} neuron pair. Significant responses (p or q \leq 0.05) are highlighted by bold borders. "Post," significant post-stimulus response; ns, no significant response.

(F-I) Average pairwise correlations between 189 neurons in the 30 s following onset of (G) NaCl, (H) 2-butanone, and (I) 2,3-pentanedione. All three correlation maps are presented on the same axes, determined by clustering the full-time-course correlations. The set of correlated and anti-correlated neurons differs for each stimulus presentation.

(J and K) Comparison of functional activity to the connectome. We observe minimal correspondence between synapse counts and pairwise-functional-activity correlations for the (J) head and (K) tail.

See Table S6 for primary data. See also Figures S1 and S2.

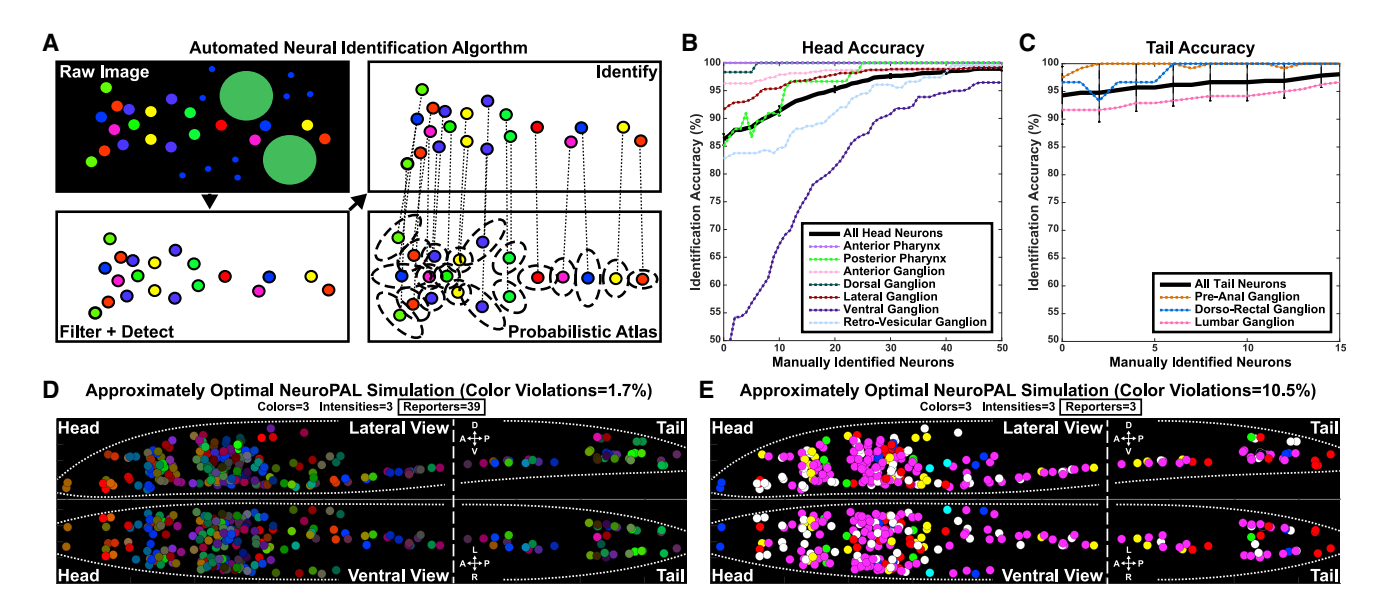


Figure 7. NeuroPAL Software: An Algorithm for Semi-automated Neuronal Identification and an Algorithm to Generate Optimal-Coloring **Solutions for Cell Identification**

(A-C) The algorithm used for semi-automated neuronal identification. (A) Raw images are filtered to remove non-neuronal fluorescence and neurons are detected in the filtered image. Detected neurons are identified by matching them to a statistical atlas of neuronal colors and positions (Table S3). (B and C) Semi-automated neuronal identification accuracy begins at 86% for the head and 94% for the tail. Manually identifying eight neurons raises the head accuracy above 90%. Overall accuracy is displayed as a black line. Accuracy for each ganglion is displayed as a dotted, colored line (see legend). Many of the neurons and ganglia have high identification accuracy and confidence. The ventral ganglion is a problematic area, likely due to the density and high positional variance therein. (D and E) The algorithm used to generate optimal-coloring solutions for cell identification—for any collection of cells in any organism. We show simulations of two approximately optimal alternatives to NeuroPAL, one that permits as many reporters as NeuroPAL (D) and one that restricts the transgene to only 3 reporters (E). With the exception of the number of reporters, both alternatives were generated using parameters similar to NeuroPAL: three landmark fluorophores, where each fluorophore is distinguishable at three intensities (high, medium, and low). Reporters were chosen by the algorithm from those available in WormBase, a community-curated database of cell-specific reporter expression. Similar databases are available for other model organisms (e.g., fly, fish, and mouse). We evaluated the two NeuroPAL alternatives by computing the percentage of their color violations, defined as neighboring neuron pairs with indistinguishable colors. See Methods S1 and S2 for algorithmic details and validation. See also Figure S3 and Table S3

non-neuronal fluorescence. Second, we detect the color and position of each neuron. Third, we compute a probabilistic estimate of each neuron's identity using a statistical atlas of NeuroPAL colors and positions (see Variability in Neuronal Cell Body Positions) (Varol et al., 2020). Last, a graphical user interface (GUI) permits manual review and error correction of all steps in our unsupervised pipeline.

We evaluated the semi-automated neuronal identification performance of our pipeline. To do so, we cross-validated its performance and found our accuracy varied across ganglia (Figures 7B and 7C). Accuracy was 86% for the head and 94% for the tail. Accuracy largely depended on neuron density; for example, our pipeline achieved high accuracy for all tail ganglia but lower accuracy for the much denser ventral ganglion in the head. Our software incorporates supervised annotation of low-probability neuronal identities to improve the estimated identities of the remaining unlabeled neurons. Adding eight manual annotations, on average, brings the head accuracy above 90% (Figure 7B).

Our algorithm also provided a means of assessing the importance of color information in assigning cell identities. When we restricted the model to assign identities only on the basis of location, automated accuracy dropped to 50% for the head and 68% for the tail (Methods S1). These results confirm a substantial improvement in accuracy with the color information provided by NeuroPAL.

An Optimal-Coloring Algorithm for Other Tissues and **Model Organisms**

We built NeuroPAL empirically, laboriously testing a large variety of reporter-fluorophore combinations. Our method can benefit research into other tissues and model organisms that require cell-specific identification. For example, in Figure S3, we suggest a design for a general-purpose "FlyPAL" that might be well suited for studying neuronal circuits in Drosophila. To facilitate the generation of further analogous multicolor landmarking solutions, for any collection of cells in any organism, we developed an algorithm that computes approximately optimal reporter-fluorophore combinations to test in vivo (Methods S2; optimal-coloring software: https://www.hobertlab.org/neuropal/). With our optimal-coloring software, the amount of empirical testing required to construct future multicolor landmarking reagents is significantly reduced.

As an overview, in order to be individually identifiable, neighboring cells of different types must be distinguishable from each other. Cells that cannot be distinguished by morphology must be distinguished by color and/or intensity differences larger than a discrimination margin. In our software, the user chooses this margin, decides which cells must be distinguishable from each other, specifies the number of landmark fluorophores to use in combination with a list of available reporters that have known expression, and restricts the total number of reporter-





fluorophore combinations permitted by their transgenesis techniques. Given these inputs, the algorithm generates multiple approximately optimal solutions (reporter-fluorophore combinations) that minimize the percentage of color violations, defined as neighboring neuron pairs that fall below the discrimination margin.

We ran our optimal-coloring algorithm using WormBase (a database of worm reporter expression) to generate several NeuroPAL alternatives (Methods S2). In our simulations, we achieve color violations of 1.7% when using 39 reporters and 10.5% when restricting the solution to only 3 reporters (Figures 7D and 7E). This low percentage of indistinguishable neurons, in our two simulated NeuroPAL alternatives, indicates that they could prove beneficial for neuronal identification.

Our algorithmic and FlyPAL examples illustrate how the NeuroPAL-technique can be extended to offer multicolor landmarking solutions for any collection of cells, in any model organism, using similar databases of reporter expression (e.g., using Fly-Base for fly, ZFIN for zebrafish, and MGI for mouse). Although transgenesis techniques in other model organisms may restrict the total number of reporters that can be used, we show that despite this limitation, our algorithm can still offer beneficial solutions to devise stereotypic color maps for cellular identification.

DISCUSSION

Understanding the nervous system requires an integrated view of its constituent molecular, cellular, and functional signaling networks. A primary bottleneck to mapping these networks across an entire brain has been the difficulty of reliably identifying neuronal cell types. Here, we introduced NeuroPAL, a tool that allows researchers to use a single multicolor landmark strain to determine all neuron identities in the *C. elegans* nervous system. NeuroPAL offers comprehensive neuronal identification, and thus substantially improves on a recently published system that identifies, with some uncertainty, less than 60% of all neurons in the *C. elegans* nervous system (Toyoshima et al., 2020).

One major challenge in understanding the molecular networks that encode the development and function of the nervous system lies in mapping gene-expression patterns that determine cell fates and characterize the effect of genetic perturbations on neuronal fate. We have shown here that NeuroPAL can be used to identify sites of gene expression and, independently, can also be used as a cell-fate marker. By detecting mutationinduced perturbations in the NeuroPAL color map of gene expression, we uncovered a neuron-fate-specific role for EOR-1/PLZF, a ubiquitously expressed and highly conserved TF. We also completed the expression pattern of the well-studied TF PAG-3/Gli, and discovered previously unknown neuronal fate alterations caused by the loss of pag-3. These findings demonstrate the effectiveness of NeuroPAL in screening for fate-specific roles of TFs. As a next step, we envision NeuroPAL being used to screen larger collections of TF-specific mutations or being used in conjunction with the comprehensive Million Mutation Project (Thompson et al., 2013) to identify genes involved in neuronal differentiation across the nervous system.

The synaptic connectivity of the *C. elegans* nervous system has been mapped by electron microscopy. However, the path-

ways of neuronal communication therein cannot be fully understood without corresponding maps of neurotransmitter and receptor expression. We used NeuroPAL to map all neurons that express every type of metabotropic neurotransmitter receptor encoded in the worm genome. We find that the breadth of the metabotropic communication network is far more extensive than previously thought. Metabotropic neurotransmitter receptors cover 97% of all neurons and are able to participate in 75% of all synaptic connections from neurotransmitter-releasing neurons. Our contribution of the map of metabotropic GABA receptor (GABA_B) expression, combined with previous work mapping the ionotropic GABA receptors (GABAA) (Bamber et al., 1999; Beg and Jorgensen, 2003; Gendrel et al., 2016; Jobson et al., 2015), completes the GABA communication network with startling results. First, GABA_B receptors are expressed in every postsynaptic partner of all GABA-releasing neurons, whereas GABAA receptors are expressed in only 60% of these "listeners." Metabotropic reception may be the most common means of GABA signaling in the worm nervous system. Second, many neurons that express GABA receptors are not postsynaptic partners of any GABAergic neuron. Previous work has shown that extrasynaptic GABA signaling can occur between specific cell types in C. elegans (Jobson et al., 2015). Our results suggest that extrasynaptic GABA signaling may be far more prevalent than previously thought. Indeed, GABA signaling may be an important means of integrating circuit activity throughout the nervous system. Only 10% of all worm neurons release GABA but 92% of all neurons express GABA receptors and yet, just 66% of this GABA-signaling network is synaptically connected. These results underscore the need for unbiased and brainwide analysis of how functional activity is shaped by neurotransmitters and receptors. We envision future work, using NeuroPAL, to map expression of the remaining aminergic and ionotropic neurotransmitter receptors (Fernandez et al., 2020).

To date, functional networks have been investigated by recording the activity of small subsets of labeled neurons. More recent work has inaugurated whole-brain activity imaging with cellular resolution (Ahrens et al., 2013; Lemon et al., 2015; Mann et al., 2017; Schrödel et al., 2013). However, the inability to reliably identify all neurons within whole-brain recordings has precluded a full picture with circuit-level details. Thus, principal component analysis (PCA) has been commonly employed to construct low-dimensional representations of brain dynamics in individual animals, but the lack of a common basis has hampered animal-to-animal comparisons (Linderman et al., 2019). Coupling NeuroPAL with whole-brain activity imaging methods, as described here, permits a unified view of network dynamics, across animals, without sacrificing circuit-level details. Our results show that the set of stimulus-evoked responses engage the nervous system far more broadly than previously realized, extending across many sensory neurons and interneurons, even those in the synaptically isolated pharyngeal nervous system. We discovered interneurons with no previously known functions exhibited significant responses to anywhere from one to all three chemosensory stimuli.

Comprehensive neuronal identification enabled us to examine the relationship between whole-brain activity and the connectome but we found no strong correlations between them.





Unifying functional and anatomical views of the nervous system will require a deeper understanding of the properties of synaptic communication and the neuromodulation of activity patterns; we expect our work to aid in these endeavors (Bargmann and Marder, 2013; Brennan and Proekt, 2019; Kaplan et al., 2020; Kato et al., 2015). A richer set of network responses, even for simple chemosensory inputs, has broad relevance in understanding sensorimotor processing. Our work indicates that even simple behaviors employ large portions of the worm nervous system, engaging different brainwide neuronal correlations across behaviors.

Using a stereotyped multicolor landmark strain to easily identify neurons may be extended to other genetically tractable animals including fruit fly and zebrafish. As their brains are considerably larger, generating multiple landmark strains that in aggregate cover their whole brain would require communitywide efforts. However, deterministic multicolor labeling of individual brain regions of interest should be tractable. Important and well-studied brain regions in these systems (e.g., the mushroom body or nerve cord of the fly and the olfactory bulb of the zebrafish) have substantial cellular diversity in a limited number of cells, making them good targets for a tool like NeuroPAL.

Limitations of Study

Neuron identification by NeuroPAL is not constrained by microscopy equipment and, with the appropriate optical filters, can be used on multiple imaging platforms. The application of Neuro-PAL to whole-nervous-system activity recording is mainly limited by nuclear localization of the GCaMP activity sensor, as this may fail to capture highly localized events in axodendritic compartments. This limitation, combined with potentially incomplete or variable anatomical synaptic annotations, may have contributed to the lack of correlation we observed between functional activity and synaptic connectivity. Incomplete or variable anatomical synaptic annotations may have also contributed to the extent of extrasynaptic communication that we extrapolated from neurotransmitter-receptor expression patterns.

STAR*METHODS

Detailed methods are provided in the online version of this paper and include the following:

- KEY RESOURCES TABLE
- RESOURCE AVAILABILITY
 - Lead Contact
 - Materials Availability
 - Data and Code Availability
- EXPERIMENTAL MODEL AND SUBJECT DETAILS
 - O Worms and maintenance
 - Plasmids and injections
 - Transgenic and mutant strains
- METHOD DETAILS
 - Worm phenotyping
 - Electron micrograph reconstruction
 - NeuroPAL imaging
 - O Identifying neuronal sites of gene expression
 - Brainwide imaging with microfluidic stimuli

- Brainwide imaging of neuronal activity traces
- QUANTIFICATION AND STATISTICAL ANALYSIS
 - Statistical analysis
 - Mutant analysis
 - Analysis of brainwide imaging data
 - Statistical analysis software
 - Additional Resources

SUPPLEMENTAL INFORMATION

Supplemental Information can be found online at https://doi.org/10.1016/j. cell.2020.12.012.

ACKNOWLEDGMENTS

We thank Qi Chen for generating transgenic lines. We thank Molly Booth Reilly, Ibnul Rafi, and Emily Berghoff for alpha testing the NeuroPAL software. We thank Eduardo Leyva-Díaz for ehs-1^{prom7} and Michael Koelle for a gbb-2 reporter fosmid. We thank David Hall, Zeynep Altun, and Chris Crocker for use of the WormAtlas N2S/T/U EM reconstructions and Steven Cook for instruction in tracing these EM reconstructions. We thank Michael Z. Lin, Vladislav Verkhusha, and Robert E. Campbell for their considerable help in choosing fluorescent proteins. We thank Benjamin White and Wesley Grueber for their considerable help conceptualizing NeuroPAL applications in Drosophila; Guangwei Si and Jessleen Kanwal for their advice on microfluidics design and operation; Scott Linderman and Andrew Leifer for many helpful discussions regarding automated neuronal identification; and members of the Hobert, Chalfie, Paninski, and Samuel labs for comments on the manuscript. Some strains were provided by the CGC, which is funded by NIH Office of Research Infrastructure Programs (P40 OD010440). Microfluidics devices were manufactured using the Soft Materials Cleanroom facility of the Harvard MRSEC (DMR-1420570). O.H. was funded by the Howard Hughes Medical Institute and NSF-CRCNS Award (1912194). E.Y. was funded in part by the NIH (5T32DK7328-37, 5T32DK007328-35, 5T32MH015174-38, and 5T32MH015174-37). L.P. was funded by the NIBIB R01 (EB22913), NSF NeuroNex Award (DBI-1707398), NSF-CRCNS Award (1912194), the Simons Collaboration on the Global Brain, and the Gatsby Charitable Foundation. G.E.M. was funded by the Harvard Data Science Initiative Postdoctoral Fellowship. A.D.T.S. was funded by the NIH (1R01NS113119-01) and NSF (IOS-1452593), A.L. by the NSF Physics of Living Systems Graduate Student Research Network (1806818), and V.V. by the Burroughs Wellcome Fund Career Award at the Scientific Interface.

AUTHOR CONTRIBUTIONS

All authors contributed in writing this manuscript. O.H. initiated the project. E.Y. designed and built NeuroPAL, designed and performed all non-stimulus behavioral phenotyping, traced the EM reconstructions, conducted all metabotropic receptor and mutant experiments, generated the panneuronal GCaMP6s strain, and performed the non-automated identification of activity traces. A.L. designed and performed all chemotactic assays. A.L., A.D.T.S., and V.V. designed and built the whole-brain imaging scope and microfluidic device then, together with E.Y. and O.H., designed the whole-brain imaging experiments that were all conducted in the A.D.T.S. lab. A.L. performed all whole-brain imaging experiments. A.N., E.V., L.P., and V.V. designed and built the software for whole-brain activity imaging that connects neurons with their identities, then extracts, de-mixes, and normalizes neuronal activity traces. A.L., E.Y., and V.V. designed and built the software to analyze the whole-brain imaging data. A.N., E.V., G.E.M., L.P., and R.S. computed the neuronal positional variability atlas, designed the semi-automated identification algorithms and software with accuracy validations, and together with E.Y. built the GUI. E.V. designed and built software to compute coloring for NeuroPAL applications and E.Y. generated the accompanying analysis. E.Y. designed the Fly-PAL concept. Correspondence about calcium imaging and physiology is to be addressed to A.L. (albertlin@g.harvard.edu), V.V. (v.venkatachalam@





northeastern.edu), and E.Y. (eiy1@columbia.edu). Correspondence about algorithms for semi-automated cell identification is to be addressed to A.N. (mn2822@columbia.edu), E.V. (ev2430@columbia.edu), and E.Y. (eiy1@columbia.edu).

DECLARATION OF INTERESTS

The authors declare no competing interests.

Received: July 2, 2019 Revised: June 30, 2020 Accepted: December 8, 2020 Published: December 29, 2020

REFERENCES

Ahrens, M.B., and Engert, F. (2015). Large-scale imaging in small brains. Curr. Opin. Neurobiol. 32, 78–86.

Ahrens, M.B., Orger, M.B., Robson, D.N., Li, J.M., and Keller, P.J. (2013). Whole-brain functional imaging at cellular resolution using light-sheet microscopy. Nat. Methods *10*, 413–420.

Bamber, B.A., Beg, A.A., Twyman, R.E., and Jorgensen, E.M. (1999). The Caenorhabditis elegans unc-49 locus encodes multiple subunits of a heteromultimeric GABA receptor. J. Neurosci. *19*, 5348–5359.

Bargmann, C.I., and Horvitz, H.R. (1991). Chemosensory neurons with overlapping functions direct chemotaxis to multiple chemicals in C. elegans. Neuron 7, 729–742.

Bargmann, C.I., and Marder, E. (2013). From the connectome to brain function. Nat. Methods *10*, 483–490.

Bargmann, C.I., Hartwieg, E., and Horvitz, H.R. (1993). Odorant-selective genes and neurons mediate olfaction in C. elegans. Cell 74, 515–527.

Bauer Huang, S.L., Saheki, Y., VanHoven, M.K., Torayama, I., Ishihara, T., Katsura, I., van der Linden, A., Sengupta, P., and Bargmann, C.I. (2007). Left-right olfactory asymmetry results from antagonistic functions of voltage-activated calcium channels and the Raw repeat protein OLRN-1 in C. elegans. Neural Dev. 2, 24

Beg, A.A., and Jorgensen, E.M. (2003). EXP-1 is an excitatory GABA-gated cation channel. Nat. Neurosci. 6, 1145–1152.

Bentley, B., Branicky, R., Barnes, C.L., Chew, Y.L., Yemini, E., Bullmore, E.T., Vértes, P.E., and Schafer, W.R. (2016). The Multilayer Connectome of Caenorhabditis elegans. PLoS Comput. Biol. *12*, e1005283.

Brand, A.H., and Perrimon, N. (1993). Targeted gene expression as a means of altering cell fates and generating dominant phenotypes. Development *118*, 401–415

Brennan, C., and Proekt, A. (2019). A quantitative model of conserved macroscopic dynamics predicts future motor commands. eLife 8, e46814.

Brenner, S. (1974). The genetics of Caenorhabditis elegans. Genetics 77, 71–94.

Bubnis, G., Ban, S., DiFranco, M.D., and Kato, S. (2019). A probabilistic atlas for cell identification. arXiv, 1903.09227.

Cameron, S., Clark, S.G., McDermott, J.B., Aamodt, E., and Horvitz, H.R. (2002). PAG-3, a Zn-finger transcription factor, determines neuroblast fate in C. elegans. Development *129*, 1763–1774.

Cardona, A., Saalfeld, S., Schindelin, J., Arganda-Carreras, I., Preibisch, S., Longair, M., Tomancak, P., Hartenstein, V., and Douglas, R.J. (2012). TrakEM2 software for neural circuit reconstruction. PLoS ONE 7, e38011.

Chalasani, S.H., Chronis, N., Tsunozaki, M., Gray, J.M., Ramot, D., Goodman, M.B., and Bargmann, C.I. (2007). Dissecting a circuit for olfactory behaviour in Caenorhabditis elegans. Nature *450*, 63–70.

Chan, J.P., Staab, T.A., Wang, H., Mazzasette, C., Butte, Z., and Sieburth, D. (2013). Extrasynaptic muscarinic acetylcholine receptors on neuronal cell bodies regulate presynaptic function in Caenorhabditis elegans. J. Neurosci. 33, 14146–14159.

Chase, D.L., and Koelle, M.R. (2004). Genetic analysis of RGS protein function in Caenorhabditis elegans. Methods Enzymol. 389, 305–320.

Chronis, N., Zimmer, M., and Bargmann, C.I. (2007). Microfluidics for in vivo imaging of neuronal and behavioral activity in Caenorhabditis elegans. Nat. Methods 4, 727–731.

Chu, J., Haynes, R.D., Corbel, S.Y., Li, P., González-González, E., Burg, J.S., Ataie, N.J., Lam, A.J., Cranfill, P.J., Baird, M.A., et al. (2014). Non-invasive intravital imaging of cellular differentiation with a bright red-excitable fluorescent protein. Nat. Methods *11*, 572–578.

Chu, J., Oh, Y., Sens, A., Ataie, N., Dana, H., Macklin, J.J., Laviv, T., Welf, E.S., Dean, K.M., Zhang, F., et al. (2016). A bright cyan-excitable orange fluorescent protein facilitates dual-emission microscopy and enhances bioluminescence imaging in vivo. Nat. Biotechnol. *34*, 760–767.

Cook, S.J., Jarrell, T.A., Brittin, C.A., Wang, Y., Bloniarz, A.E., Yakovlev, M.A., Nguyen, K.C.Q., Tang, L.T., Bayer, E.A., Duerr, J.S., et al. (2019). Whole-animal connectomes of both Caenorhabditis elegans sexes. Nature *571*, 63–71.

Cook, S.J., Crouse, C.M., Yemini, E., Hall, D.H., Emmons, S.W., and Hobert, O. (2020). The connectome of the Caenorhabditis elegans pharynx. J. Comp. Neurol. *528*, 2767–2784.

Diao, F., Elliott, A.D., Diao, F., Shah, S., and White, B.H. (2017). Neuromodulatory connectivity defines the structure of a behavioral neural network. eLife 6, e29797.

Etchberger, J.F., and Hobert, O. (2008). Vector-free DNA constructs improve transgene expression in C. elegans. Nat. Methods 5, 3.

Fernandez, R.W., Wei, K., Wang, E.Y., Mikalauskaite, D., Olson, A., Pepper, J.S., Christie, N., Kim, S., and Koelle, M.R. (2020). Cellular expression and functional roles of all 26 neurotransmitter GPCRs in the C. elegans egg-laying circuit. bioRxiv. https://doi.org/10.1101/2020.04.23.037242.

Fouad, A.D., Teng, S., Mark, J.R., Liu, A., Alvarez-Illera, P., Ji, H., Du, A., Bhirgoo, P.D., Cornblath, E., Guan, S.A., and Fang-Yen, C. (2018). Distributed rhythm generators underlie *Caenorhabditis elegans* forward locomotion. eLife 7. e29913.

Gendrel, M., Atlas, E.G., and Hobert, O. (2016). A cellular and regulatory map of the GABAergic nervous system of *C. elegans*. eLife 5, e17686.

Granato, M., Schnabel, H., and Schnabel, R. (1994). pha-1, a selectable marker for gene transfer in C. elegans. Nucleic Acids Res. 22, 1762–1763.

Hall, D.H., and Altun, Z. (2007). C. Elegans Atlas (Cold Spring Harbor Laboratory Press).

Hardaker, L.A., Singer, E., Kerr, R., Zhou, G., and Schafer, W.R. (2001). Serotonin modulates locomotory behavior and coordinates egg-laying and movement in Caenorhabditis elegans. J. Neurobiol. 49, 303–313.

Hedgecock, E.M., Culotti, J.G., Thomson, J.N., and Perkins, L.A. (1985). Axonal guidance mutants of Caenorhabditis elegans identified by filling sensory neurons with fluorescein dyes. Dev. Biol. *111*, 158–170.

Hilliard, M.A., Bargmann, C.I., and Bazzicalupo, P. (2002). C. elegans responds to chemical repellents by integrating sensory inputs from the head and the tail. Curr. Biol. 12, 730–734.

Hobert, O. (2002). PCR fusion-based approach to create reporter gene constructs for expression analysis in transgenic C. elegans. Biotechniques *32*, 728–730.

Hobert, O. (2013). The neuronal genome of Caenorhabditis elegans. Worm-Book. 1–106.

Howard, R.M., and Sundaram, M.V. (2002). C. elegans EOR-1/PLZF and EOR-2 positively regulate Ras and Wnt signaling and function redundantly with LIN-25 and the SUR-2 Mediator component. Genes Dev. *16*, 1815–1827.

Jobson, M.A., Valdez, C.M., Gardner, J., Garcia, L.R., Jorgensen, E.M., and Beg, A.A. (2015). Spillover transmission is mediated by the excitatory GABA receptor LGC-35 in C. elegans. J. Neurosci. *35*, 2803–2816.

Jones, A.R., Overly, C.C., and Sunkin, S.M. (2009). The Allen Brain Atlas: 5 years and beyond. Nat. Rev. Neurosci. 10, 821–828.

Kakidani, H., and Ptashne, M. (1988). GAL4 activates gene expression in mammalian cells. Cell 52, 161–167.





Kaplan, H.S., Salazar Thula, O., Khoss, N., and Zimmer, M. (2020). Nested Neuronal Dynamics Orchestrate a Behavioral Hierarchy across Timescales. Neuron 105, 562-576.e9.

Kato, S., Kaplan, H.S., Schrödel, T., Skora, S., Lindsay, T.H., Yemini, E., Lockery, S., and Zimmer, M. (2015). Global brain dynamics embed the motor command sequence of Caenorhabditis elegans. Cell 163, 656-669.

Kim, Y.J., Zitnan, D., Galizia, C.G., Cho, K.H., and Adams, M.E. (2006). A command chemical triggers an innate behavior by sequential activation of multiple peptidergic ensembles. Curr. Biol. 16, 1395-1407.

Kotera, I., Tran, N.A., Fu, D., Kim, J.H., Byrne Rodgers, J., and Ryu, W.S. (2016). Pan-neuronal screening in Caenorhabditis elegans reveals asymmetric dynamics of AWC neurons is critical for thermal avoidance behavior. eLife 5, e19021.

Lai, S.L., and Lee, T. (2006). Genetic mosaic with dual binary transcriptional systems in Drosophila. Nat. Neurosci. 9, 703-709.

Larsch, J., Ventimiglia, D., Bargmann, C.I., and Albrecht, D.R. (2013). Highthroughput imaging of neuronal activity in Caenorhabditis elegans. Proc. Natl. Acad. Sci. USA 110, E4266-E4273.

Lemon, W.C., Pulver, S.R., Höckendorf, B., McDole, K., Branson, K., Freeman, J., and Keller, P.J. (2015). Whole-central nervous system functional imaging in larval Drosophila. Nat. Commun. 6, 7924.

Lichtman, J.W., and Denk, W. (2011). The big and the small: challenges of imaging the brain's circuits. Science 334, 618-623.

Linderman, S., Nichols, A., Blei, D., Zimmer, M., and Paninski, L. (2019). Hierarchical recurrent state space models reveal discrete and continuous dynamics of neural activity in C. elegans. bioRxiv. https://doi.org/10.1101/

Linkert, M., Rueden, C.T., Allan, C., Burel, J.M., Moore, W., Patterson, A., Loranger, B., Moore, J., Neves, C., Macdonald, D., et al. (2010). Metadata matters: access to image data in the real world. J. Cell Biol. 189, 777-782.

Livet, J., Weissman, T.A., Kang, H., Draft, R.W., Lu, J., Bennis, R.A., Sanes, J.R., and Lichtman, J.W. (2007). Transgenic strategies for combinatorial expression of fluorescent proteins in the nervous system. Nature 450, 56-62.

Mann, K., Gallen, C.L., and Clandinin, T.R. (2017). Whole-Brain Calcium Imaging Reveals an Intrinsic Functional Network in Drosophila. Curr. Biol. 27, 2389-2396 e4

MathWorks (2019). MATLAB and Statistics Toolbox Release, Vol. R2019b (The MathWorks, Inc.).

Nejatbakhsh, A., Varol, E., Yemini, E., Venkatachalam, V., Lin, A., Samuel, A., and Paninski, L. (2020). Extracting neural signals from semi-immobilized animals with deformable non-negative matrix factorization. bioRxiv. https://doi. org/10.1101/2020.07.07.192120.

Nguyen, J.P., Shipley, F.B., Linder, A.N., Plummer, G.S., Liu, M., Setru, S.U., Shaevitz, J.W., and Leifer, A.M. (2016). Whole-brain calcium imaging with cellular resolution in freely behaving Caenorhabditis elegans. Proc. Natl. Acad. Sci. USA 113, E1074-E1081.

Ortiz, C.O., Faumont, S., Takayama, J., Ahmed, H.K., Goldsmith, A.D., Pocock, R., McCormick, K.E., Kunimoto, H., Iino, Y., Lockery, S., and Hobert, O. (2009). Lateralized gustatory behavior of C. elegans is controlled by specific receptor-type guanylyl cyclases. Curr. Biol. 19, 996-1004.

Pereira, L., Kratsios, P., Serrano-Saiz, E., Sheftel, H., Mayo, A.E., Hall, D.H., White, J.G., LeBoeuf, B., Garcia, L.R., Alon, U., and Hobert, O. (2015). A cellular and regulatory map of the cholinergic nervous system of C. elegans. eLife 4, e17686.

Pierce-Shimomura, J.T., Faumont, S., Gaston, M.R., Pearson, B.J., and Lockery, S.R. (2001). The homeobox gene lim-6 is required for distinct chemosensory representations in C. elegans. Nature 410, 694-698.

Potter, C.J., Tasic, B., Russler, E.V., Liang, L., and Luo, L. (2010). The Q system: a repressible binary system for transgene expression, lineage tracing, and mosaic analysis. Cell 141, 536-548.

Richier, B., and Salecker, I. (2015). Versatile genetic paintbrushes: Brainbow technologies. Wiley Interdiscip. Rev. Dev. Biol. 4, 161-180.

Sarov, M., Murray, J.I., Schanze, K., Pozniakovski, A., Niu, W., Angermann, K., Hasse, S., Rupprecht, M., Vinis, E., Tinney, M., et al. (2012). A genome-scale resource for in vivo tag-based protein function exploration in C. elegans. Cell 150, 855-866.

Schindelin, J., Arganda-Carreras, I., Frise, E., Kaynig, V., Longair, M., Pietzsch, T., Preibisch, S., Rueden, C., Saalfeld, S., Schmid, B., et al. (2012). Fiji: an open-source platform for biological-image analysis. Nat. Methods 9, 676–682.

Schrödel, T., Prevedel, R., Aumayr, K., Zimmer, M., and Vaziri, A. (2013). Brainwide 3D imaging of neuronal activity in Caenorhabditis elegans with sculpted light. Nat. Methods 10, 1013-1020.

Serrano-Saiz, E., Poole, R.J., Felton, T., Zhang, F., De La Cruz, E.D., and Hobert, O. (2013). Modular control of glutamatergic neuronal identity in C. elegans by distinct homeodomain proteins. Cell 155, 659-673.

Shaner, N.C., Lin, M.Z., McKeown, M.R., Steinbach, P.A., Hazelwood, K.L., Davidson, M.W., and Tsien, R.Y. (2008). Improving the photostability of bright monomeric orange and red fluorescent proteins. Nat. Methods 5, 545-551.

Si, G., Kanwal, J.K., Hu, Y., Tabone, C.J., Baron, J., Berck, M., Vignoud, G., and Samuel, A.D.T. (2019). Structured Odorant Response Patterns across a Complete Olfactory Receptor Neuron Population. Neuron 101, 950-962.e7.

Stefanakis, N., Carrera, I., and Hobert, O. (2015). Regulatory Logic of Pan-Neuronal Gene Expression in C. elegans. Neuron 87, 733-750.

Storey, J.D. (2002). A Direct Approach to False Discovery Rates. J. R. Stat. Soc. Ser. A Stat. Soc. 64, 479-498.

Subach, O.M., Cranfill, P.J., Davidson, M.W., and Verkhusha, V.V. (2011). An enhanced monomeric blue fluorescent protein with the high chemical stability of the chromophore. PLoS ONE 6, e28674.

Sulston, J.E. (1983), Neuronal cell lineages in the nematode Caenorhabditis elegans. Cold Spring Harb. Symp. Quant. Biol. 48, 443-452.

Suzuki, H., Thiele, T.R., Faumont, S., Ezcurra, M., Lockery, S.R., and Schafer, W.R. (2008). Functional asymmetry in Caenorhabditis elegans taste neurons and its computational role in chemotaxis. Nature 454, 114–117.

Thiele, T.R., Faumont, S., and Lockery, S.R. (2009). The neural network for chemotaxis to tastants in Caenorhabditis elegans is specialized for temporal differentiation, J. Neurosci. 29, 11904-11911.

Thompson, O., Edgley, M., Strasbourger, P., Flibotte, S., Ewing, B., Adair, R., Au, V., Chaudhry, I., Fernando, L., Hutter, H., et al. (2013). The million mutation project: a new approach to genetics in Caenorhabditis elegans. Genome Res. 23. 1749-1762.

Toyoshima, Y., Wu, S., Kanamori, M., Sato, H., Jang, M.S., Oe, S., Murakami, Y., Teramoto, T., Park, C., Iwasaki, Y., et al. (2020). Neuron ID dataset facilitates neuronal annotation for whole-brain activity imaging of C. elegans. BMC Biol. 18, 30.

Varol, E., Nejatbakhsh, A., Yemini, E., Sun, R., Mena, G.E., Hobert, O., and Paninski, L. (2020). Statistical atlas of C. elegans neurons. In Medical Image Computing and Computer Assisted Intervention-MICCAI 2020, A.L. Martel, P. Abolmaesumi, D. Stoyanov, D. Mateus, M.A. Zuluaga, S.K. Zhou, D. Racoceanu, and L. Joskowicz, eds. (Springer, Cham.) https://doi.org/10.1007/978-3-030-59722-1 12.

Venkatachalam, V., Ji, N., Wang, X., Clark, C., Mitchell, J.K., Klein, M., Tabone, C.J., Florman, J., Ji, H., Greenwood, J., et al. (2016). Pan-neuronal imaging in roaming Caenorhabditis elegans. Proc. Natl. Acad. Sci. USA 113, E1082-E1088.

Ward, S. (1973). Chemotaxis by the nematode Caenorhabditis elegans: identification of attractants and analysis of the response by use of mutants. Proc. Natl. Acad. Sci. USA 70, 817-821.

Weissman, T.A., and Pan, Y.A. (2015). Brainbow: new resources and emerging biological applications for multicolor genetic labeling and analysis. Genetics

Wes, P.D., and Bargmann, C.I. (2001). C. elegans odour discrimination requires asymmetric diversity in olfactory neurons. Nature 410, 698-701.

White, J.G., Southgate, E., Thomson, J.N., and Brenner, S. (1986). The structure of the nervous system of the nematode Caenorhabditis elegans. Philos. Trans. R. Soc. Lond. B Biol. Sci. 314, 1-340.





Yemini, E., Jucikas, T., Grundy, L.J., Brown, A.E., and Schafer, W.R. (2013). A database of Caenorhabditis elegans behavioral phenotypes. Nat. Methods 10,

Zaslaver, A., Liani, I., Shtangel, O., Ginzburg, S., Yee, L., and Sternberg, P.W. (2015). Hierarchical sparse coding in the sensory system of Caenorhabditis elegans. Proc. Natl. Acad. Sci. USA 112, 1185-1189.

Zeng, H., and Sanes, J.R. (2017). Neuronal cell-type classification: challenges, opportunities and the path forward. Nat. Rev. Neurosci. 18, 530-546. Zhong, M., Niu, W., Lu, Z.J., Sarov, M., Murray, J.I., Janette, J., Raha, D., Sheaffer, K.L., Lam, H.Y., Preston, E., et al. (2010). Genome-wide identification of binding sites defines distinct functions for Caenorhabditis elegans PHA-4/ FOXA in development and environmental response. PLoS Genet. 6, e1000848.





STAR***METHODS**

KEY RESOURCES TABLE

REAGENT or RESOURCE	SOURCE	IDENTIFIER
Chemicals, Peptides, and Recombinant Proteins		
2-butanone	Sigma-Aldrich	02469; CAS: 78-93-3
2,3-pentanedione	Sigma-Aldrich	818555; CAS: 600-14-6
NaCl	BDH Chemicals	9286; CAS: 7647-14-5
Tetramisole hydrochloride	Sigma-Aldrich	L9756; CAS: 16595-80-5
Sodium azide	Sigma-Aldrich	71289; CAS: 26628-22-8
K ₂ HPO ₄	EMD Chemicals	PX1570; CAS: 7758-11-4
KH ₂ PO ₄	EMD Chemicals	PX1562; CAS: 7778-77-0
MgSO ₄	Sigma-Aldrich	M2643; CAS: 7487-88-9
CaCl ₂	Sigma-Aldrich	C5670; CAS: 10043-52-4
Sorbitol	Alfa Aesar	36404; CAS: 50-70-4
Invitrogen Vybrant DiO Cell-Labeling Solution	Thermo Fisher Scientific	V22886; CAS: 34215-57-1
Bacterial and Virus Strains		
E. coli	Caenorhabditis Genetics Center (CGC)	WormBase: OP50; WormBase: WBStrain00041969
Deposited Data		
Imaging datasets and whole-brain calcium activity	This paper	https://zenodo.org/ record/3906530
Experimental Models: Organisms/Strains		
C. elegans: Strain N2	Caenorhabditis Genetics Center	WormBase: N2; WormBase: WBStrain00000001
otEx7057[NeuroPAL]	This paper	OH15205
otls668 [NeuroPAL] V	This paper	OH15261
otls669 [NeuroPAL] V	This paper	OH15262
otls670 [NeuroPAL] V	This paper	OH15263
otls696 [NeuroPAL] not V	This paper	OH15495
otEx7056[rab-3(xATG)::3xNLS::ceGCaMP6s 32ng/ul + arrd-4(1.6K)::3xNLS::ceGCaMP6s 32ng/ul + OP50 55ng/ul]	This paper	OH15204
otls671[rab-3(xATG)::3xNLS::ceGCaMP6s 32ng/ul + arrd- 4(1.6K)::3xNLS::ceGCaMP6s 32ng/ul + OP50 55ng/ul]	This paper	OH15264
otls672[rab-3(xATG)::3xNLS::ceGCaMP6s 32ng/ul + arrd- 4(1.6K)::3xNLS::ceGCaMP6s 32ng/ul + OP50 55ng/ul]	This paper	OH15265
otls673[rab-3(xATG)::3xNLS::ceGCaMP6s 32ng/ul + arrd- 4(1.6K)::3xNLS::ceGCaMP6s 32ng/ul + OP50 55ng/ul]	This paper	OH15266
otls668[NeuroPAL]; him-5(e1490)	This paper	OH15362
otls669[NeuroPAL]; him-5(e1490)	This paper	OH15363
otls670[NeuroPAL]; him-8(e1489)	This paper	OH16298
otls696[NeuroPAL]; him-5(e1490)	This paper	OH15528
otls669[NeuroPAL]; otls672[panneuronal::GCaMP6s]	This paper	OH15368
otls669[NeuroPAL]; otls672[panneuronal::GCaMP6s]	This paper	OH15500
otls670[NeuroPAL]; otls672[panneuronal::GCaMP6s]	This paper	OH16230
otls669[NeuroPAL];pha-1(e2123)	This paper	OH15430
otls670[NeuroPAL];pha-1(e2123)	This paper	OH15431
		(Continued on next page

(Continued on next page)





Continued			
REAGENT or RESOURCE	SOURCE	IDENTIFIER	
otEx7216[gar-1(fosmid)::GFP 5ng/ul + inx- 6(prom18)::TagRFP 7ng/ul + pha-1(+) 3ng/ul + OP50 100ng/ul]; otIs669[NeuroPAL]; pha-1(e2123)	This paper	OH15519	
otEx7217[gar-1(fosmid)::GFP 5ng/ul + inx- 6(prom18)::TagRFP 7ng/ul + pha-1(+) 3ng/ul + OP50 100ng/ul]; otIs669[NeuroPAL]; pha-1(e2123)	This paper	OH15520	
otEx7218[gar-1(fosmid)::GFP 5ng/ul + inx- 6(prom18)::TagRFP 7ng/ul + pha-1(+) 3ng/ul + OP50 100ng/ul]; otls669[NeuroPAL]; pha-1(e2123)	This paper	OH15521	
otEx7209[gar-2(fosmid)::GFP 5ng/ul + inx- 6(prom18)::TagRFP 7ng/ul + pha-1(+) 3ng/ul + OP50 100ng/ul]; otls669[NeuroPAL]; pha-1(e2123)	This paper	OH15511	
otEx7210[gar-2(fosmid)::GFP 5ng/ul + inx- 6(prom18)::TagRFP 7ng/ul + pha-1(+) 3ng/ul + OP50 100ng/ul]; otIs669[NeuroPAL]; pha-1(e2123)	This paper	OH15512	
otEx7211[gar-2(fosmid)::GFP 5ng/ul + inx- 6(prom18)::TagRFP 7ng/ul + pha-1(+) 3ng/ul + OP50 100ng/ul]; otIs669[NeuroPAL]; pha-1(e2123)	This paper	OH15513	
otEx7212[gar-2(fosmid)::GFP 5ng/ul + inx- 6(prom18)::TagRFP 7ng/ul + pha-1(+) 3ng/ul + OP50 100ng/ul]; otIs669[NeuroPAL]; pha-1(e2123)	This paper	OH15514	
vjEx601[gar-3(8.5kb)::GFP]; otls669[NeuroPAL]	This paper	OH15425	
otEx7201[gbb-1(fosmid)::GFP 5ng/ul + inx- 6(prom18)::TagRFP 7ng/ul + pha-1(+) 3ng/ul + OP50 100ng/ul]; otIs669[NeuroPAL]; pha-1(e2123)	This paper	OH15492	
otEx7202[gbb-1(fosmid)::GFP 5ng/ul + inx- 6(prom18)::TagRFP 7ng/ul + pha-1(+) 3ng/ul + OP50 100ng/ul]; otls669[NeuroPAL]; pha-1(e2123)	This paper	OH15493	
otEx7203[gbb-1(fosmid)::GFP 5ng/ul + inx- 6(prom18)::TagRFP 7ng/ul + pha-1(+) 3ng/ul + OP50 100ng/ul]; otls669[NeuroPAL]; pha-1(e2123)	This paper	OH15494	
vsls267[gbb-2(fosmid)::GFP + lin-15(+)];otls696 [NeuroPAL];	This paper	OH15887	
otEx7204[mgl-1(fosmid)::GFP 5ng/ul + inx- 6(prom18)::TagRFP 7ng/ul + pha-1(+) 3ng/ul + OP50 100ng/ul]; otls669[NeuroPAL]; pha-1(e2123)	This paper	OH15497	
otEx7205[mgl-1(fosmid)::GFP 5ng/ul + inx- 6(prom18)::TagRFP 7ng/ul + pha-1(+) 3ng/ul + OP50 100ng/ul]; otIs669[NeuroPAL]; pha-1(e2123)	This paper	OH15498	
otEx7206[mgl-1(fosmid)::GFP 5ng/ul + inx- 6(prom18)::TagRFP 7ng/ul + pha-1(+) 3ng/ul + OP50 100ng/ul]; otls669[NeuroPAL]; pha-1(e2123)	This paper	OH15499	
otEx7243[mgl-2(7.9kb)::GFP 30ng/ul + inx- 6(prom18)::TagRFP 40ng/ul + pha-1(+) 30ng/ul]; otls669 [NeuroPAL]; pha-1(e2123)	This paper	OH15554	
otEx7244[mgl-2(7.9kb)::GFP 30ng/ul + inx- 6(prom18)::TagRFP 40ng/ul + pha-1(+) 30ng/ul]; otIs669 [NeuroPAL]; pha-1(e2123)	This paper	OH15555	
otEx7245[mgl-2(7.9kb)::GFP 30ng/ul + inx- 6(prom18)::TagRFP 40ng/ul + pha-1(+) 30ng/ul]; otls669 [NeuroPAL]; pha-1(e2123)	This paper	OH15556	
otEx7213[mgl-3(fosmid)::GFP 5ng/ul + inx- 6(prom18)::TagRFP 7ng/ul + pha-1(+) 3ng/ul + OP50 100ng/ul]; otIs669[NeuroPAL]; pha-1(e2123)	This paper	OH15516	

(Continued on next page)





Continued		
REAGENT or RESOURCE	SOURCE	IDENTIFIER
otEx7214[mgl-3(fosmid)::GFP 5ng/ul + inx- 6(prom18)::TagRFP 7ng/ul + pha-1(+) 3ng/ul + OP50 100ng/ul]; otIs669[NeuroPAL]; pha-1(e2123)	This paper	OH15517
otEx7215[mgl-3(fosmid)::GFP 5ng/ul + inx- 6(prom18)::TagRFP 7ng/ul + pha-1(+) 3ng/ul + OP50 100ng/ul]; otls669[NeuroPAL]; pha-1(e2123)	This paper	OH15518
otEx7240[maf-1(fosmid)::GFP 7ng/ul + inx- 6(prom18)::TagRFP 6ng/ul + pha-1(+) 3ng/ul + OP50 100ng/ul]; otls669[NeuroPAL]; pha-1(e2123)	This paper	OH15551
otEx7241[maf-1(fosmid)::GFP 7ng/ul + inx- 6(prom18)::TagRFP 6ng/ul + pha-1(+) 3ng/ul + OP50 100ng/ul]; otIs669[NeuroPAL]; pha-1(e2123)	This paper	OH15552
otEx7242[maf-1(fosmid)::GFP 7ng/ul + inx- 6(prom18)::TagRFP 6ng/ul + pha-1(+) 3ng/ul + OP50 00ng/ul]; otls669[NeuroPAL]; pha-1(e2123)	This paper	OH15553
otls669[NeuroPAL];wgls81[eor-1::TY1::EGFP::3xFLAG + unc-119(+)]	This paper	OH15700
otls669[NeuroPAL];eor-1(cs28)	This paper	OH15753
otls669[NeuroPAL];eor-1(ok1127)	This paper	OH15701
otls514[pMG89 (unc- 25p(1.8kb)::unc25(UPto6thexon)::GFP::unc54_3'UTR) + pha-1(+)]; otls565[fMG1(unc- 47(fosmid)::SL2::H2B::mCHOPTI) + pha-1(+)]IV; him- 5(e1490)V	Gendrel et al., 2016	OH13334
eor-1(cs28)IV; otls514[pMG89 (unc- 25p(1.8kb)::unc25(UPto6thexon)::GFP::unc54_3'UTR) + oha-1(+)]; otls565[fMG1(unc- 47(fosmid)::SL2::H2B::mCHOPTI) + pha-1(+)]IV	This paper	OH15777
eor-1(ok1127)IV; otls514[pMG89 (unc- 25p(1.8kb)::unc25(UPto6thexon)::GFP::unc54_3'UTR) + oha-1(+)]; otls565[fMG1(unc- 47(fosmid)::SL2::H2B::mCHOPTI) + pha-1(+)]IV	This paper	OH15769
otls669[NeuroPAL];wgls154[pag- 3::TY1::EGFP::3xFLAG + unc-119(+)]	This paper	OH15729
otls669[NeuroPAL];pag-3(n3098)	This paper	OH15770
ntls669[NeuroPAL];pag-3(ok488)	This paper	OH15730
Dligonucleotides		
Primers for fluorescent reporters, see Tables S1 and S4	This paper	N/A
Software and Algorithms		
Vorm Tracker v2.0	Yemini et al., 2013	https://www.mrc-lmb.cam.ac.uk/wormtracker
MATLAB	MathWorks	R2019b
NeuroPAL Automated Cell ID	This paper	https://github.com/amin-nejat/CELL_ID
NeuroPAL Optimal Coloring	This paper	https://github.com/Eviatar/Optimal_Coloring
NeuroPAL Neuronal Traces	This paper	https://github.com/venkatachalamlab/ NeuroPAL-traces
NMF Demixed Neuronal Traces	Nejatbakhsh et al., 2020	https://github.com/amin-nejat/dNMF
DME Bio-Formats MATLAB v6.3.1	Linkert et al., 2010	https://www.openmicroscopy.org/ bio-formats/downloads/
-iji v2	(Schindelin et al., 2012)	https://imagej.net/Fiji
ΓrakEM2	Cardona et al., 2012	https://imagej.net/TrakEM2
Other		
Confocal Laser Scanning Microscope	Zeiss	LSM 880
Spinning Disk Confocal	Nikon	Ti-e

(Continued on next page)





Continued		
REAGENT or RESOURCE	SOURCE	IDENTIFIER
EMCCD Camera	Andor	iXon Ultra 897
EMCCD Camera	Andor	iXon DU-897
60x Objective, 1.2 NA	Nikon	CFI Plan Apochromat VC 60XC WI
FF01-445/45-25 Brightline (420-470 nm bandpass)	Semrock	FF01-445/45-25
FF02-525/40-25 Brightline (500-545 nm bandpass)	Semrock	FF02-525/40-25
FF02-617/73-25 Brightline (570-650 nm bandpass)	Semrock	FF02-617/73-25
FF01-731/137-25 Brightline (660-800 nm bandpass)	Semrock	FF01-731/137-25

RESOURCE AVAILABILITY

Lead Contact

Further information and requests for resources and reagents should be directed to and will be fulfilled by the Lead Contact, Eviatar Yemini (eiy1@columbia.edu).

Materials Availability

The extrachromosomal and integrant NeuroPAL transgenes, panneuronal GCaMP6s integrants, extrachromosomal metabotropic neurotransmitter receptor reporters, and several other useful C. elegans strains generated in this study (Tables S1 and S4; Key Resources Table) are available at the Caenorhabditis Genetics Center (CGC).

Data and Code Availability

The accession number for the imaging datasets and whole-brain calcium activity reported in this paper (Figures 2C-2D, 6, 7, S1H, and S2; Tables S3 and S6; Methods S1 and S2) is Zenodo repository: https://doi.org/10.5281/zenodo.3906530

The code and software generated during this study (Figure 7; Tables S3 and S6; Methods S1 and S2) use MATLAB (MathWorks, 2019) and Bio-Formats OME (Linkert et al., 2010) and are available at:

https://github.com/amin-nejat/CELL_ID https://github.com/Eviatar/Optimal_Coloring https://github.com/venkatachalamlab/NeuroPAL-traces/ https://www.hobertlab.org/neuropal/

EXPERIMENTAL MODEL AND SUBJECT DETAILS

Worms and maintenance

All Caenorhabditis elegans were raised at 20°C, on nematode growth media (NGM) plates, and fed OP50 Escherichia coli as previously described (Brenner, 1974), unless otherwise noted. Strains with a pha-1 mutant background were raised at 25°C for selection. Wild-type C. elegans were Bristol, strain N2. All C. elegans were L4 or young-adult hermaphrodites, as noted.

Plasmids and injections

Fluorophores were ordered from IDT and/or cloned via standard techniques (Gibson, restriction-free, T4 ligase, or QuikChange mutagenesis) into the pPD95.62 Fire vector (a gift from Andrew Fire). The 1.4 kb synthetic ultra-panneuronal driver (UPN) was generated by fusing cis-regulatory elements from four different panneuronally expressed genes: unc-11^{prom8}, rgef-1^{prom2}, ehs-1^{prom7}, ric-19^{prom6} (Stefanakis et al., 2015). Fusion was done in a single quadruple PCR promoter fusion (Hobert, 2002). All cloned NeuroPAL reporters were made via PCR, gel purified, then inserted using standard techniques into the fluorophore vectors. To accommodate the large number of reporters and conserve space in extrachromosomal arrays, in place of plasmid backbones we used linear DNA amplified via PCR. Linear DNA has also been shown to improve expression levels (Etchberger and Hobert, 2008). Therefore, all injected Neuro-PAL reporters were PCR amplified and gel purified to remove their vector backbone. Injection mixes consisted of complex arrays, with sheared bacterial DNA serving as spacers, to minimize potential crosstalk among reporters. Preliminary NeuroPAL strains were injected as complex arrays into pha-1(e2123) with pBX[pha-1(+)] to rescue at the selection temperature 25°C (Granato et al., 1994). Final NeuroPAL strains were injected into the wild-type, N2, without pha-1(+). We used the rab-3 reporter to drive panneuronal GCaMP6s expression. We noted that sensory neurons exhibited weaker GCaMP6s expression and thus supplemented the rab-3 reporter with the arrd-4 pansensory reporter. The panneuronal GCaMP6s reporters were injected as complex arrays into N2. Integrations were performed using gamma irradiation. All integrant worms were outcrossed 8x. Non-integrant strains that were used to identify metabotropic and transcription factor expression were injected with pAB1[inx-6^{prom18}::TagRFP-T] (an anterior pharyngeal





marker) and pBX[pha-1(+)] into pha-1(e2123), then raised at 25°C for selection. All reporters and their injected concentrations are in Tables S1 and S4.

Transgenic and mutant strains

Transgenic and mutant strains used in this study are available in the supplement (Tables S1, S4, and S5) and Key Resources Table.

METHOD DETAILS

Worm phenotyping

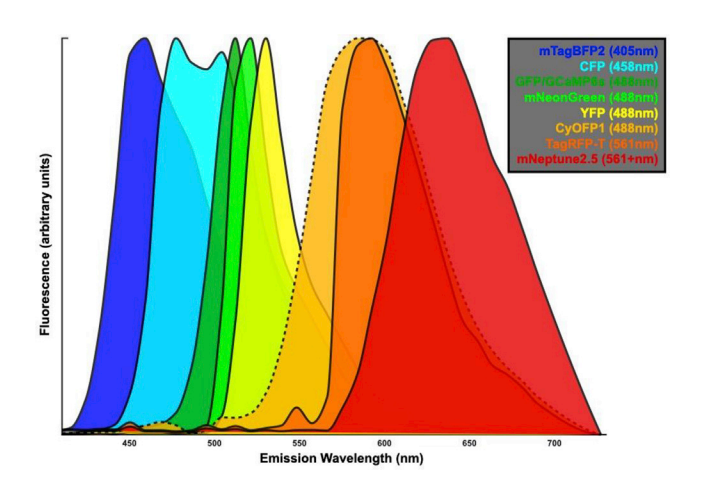
Brood-size quantification, high-resolution behavioral phenotyping, dye-fill with DiO, chemotactic quadrant assays, and drop-test assays (Figures S1A-S1G; Table S2) were performed using standard protocols (Bargmann et al., 1993; Chase and Koelle, 2004; Hedgecock et al., 1985; Hilliard et al., 2002; Yemini et al., 2013). High-resolution behavioral phenotyping was performed using L4 hermaphrodites. Dye-filling was observed in L4 to adult hermaphrodites. All chemotaxis and drop-test assays were performed on young-adult hermaphrodites. These studies were not blinded.

Electron micrograph reconstruction

Electron micrographs (Figure 2A) were obtained from WormAtlas (Hall and Altun, 2007) and reconstructed using Fiji (Schindelin et al., 2012) and TrakEM2 (Cardona et al., 2012).

NeuroPAL imaging

NeuroPAL imaging can be performed using a wide variety of microscopes as further detailed in the manual "Configuring Your Microscope for NeuroPAL" (NeuroPAL Manuals: https://www.hobertlab.org/neuropal/). We imaged strains with a Zeiss LSM880, equipped with 7 laser lines: 405, 458, 488, 514, 561, 594, and 633 nm. Our standard configuration employed 405, 488, 561, and 633 nm to excite mTagBFP2, GFP/GCaMP + CyOFP1, TagRFP-T, and mNeptune2.5, respectively. The 8-color emission spectra (below) was captured using strains that expressed each fluorophore individually.



For these, we used the LSM880's "lambda mode," employing its 32-channel spectral detector to capture color spectra from 391-727nm, at \sim 10 nm color resolution – several fluorophores were imaged by exciting them with wavelengths below peak excitation and significantly increasing both the laser power and gain. To that end, for the 8-color emission spectra, we used: 405 nm to excite mTagBFP2, CFP, GFP, and CyOFP1; 488 nm to excite YFP and mNeonGreen; and, 561 nm to excite TagRFP-T and mNeptune2.5. All NeuroPAL, reporter crosses, and mutant crosses (Figures 1E, 2B-2D, 3, and 5; Videos S1 and S2) were imaged with the same scope. When not performing a DIC overlay, gamma correction of ~0.5 was applied to images so as to improve color visibility. Occasionally, histograms were adjusted to balance colors for visibility. These image adjustments are necessary and suggested for NeuroPAL identification in order to deal with a variable range of GFP/CFP/YFP reporters and color alterations in mutant backgrounds.

Identifying neuronal sites of gene expression

To identify neuronal sites of gene expression, we used L4 and young-adult hermaphrodites. When available we used translational fosmid reporters (eor-1, gar-1, gar-2, gbb-1, gbb-2, mgl-1, mgl-3, pag-3 - Figures 3 and 5; Tables S4 and S5) (Sarov et al., 2012). The eor-1, gbb-2, and pag-3 fosmid reporters are chromosomally integrated versions of extrachromosomal arrays that had been





previously reported (Fernandez et al., 2020; Zhong et al., 2010). The gar-1, gar-2, gbb-1, mgl-1, and mgl-3 fosmid reporters were generated by modENCODE (Sarov et al., 2012). We injected these reporters with pAB1[inx-6^{prom18}::TagRFP-T] and pBX[pha-1(+)] into otls669[NeuroPAL];pha-1(e2123) (strain OH15430) (Table S1), then raised the worms at 25°C for selection. When fosmid reporters were too dim or unavailable, we used cytoplasmic 5' transcriptional reporters (gar-3, mgl-2) (Figure 3; Table S4). The gar-3 transcriptional reporter included 8.5kb of the 13.3kb intergenic region 5' to its open reading frame (ORF) (Chan et al., 2013) and the mgl-2 transcriptional reporter included the entire 7.9kb intergenic region 5' to its ORF.

Brainwide imaging with microfluidic stimuli

To record whole-brain neuronal activity, while presenting an animal with chemosensory stimuli, we employed a modified version of a microfluidic system that delivers multiple odors to Drosophila larvae (Si et al., 2019). We adapted this system for use with C. elegans (Chronis et al., 2007). This microfluidic chip allowed us to record intact animals while presenting precisely timed stimuli (Figures 6A and 6B; Videos S3 and S4). To control for the age of the animals used in these experiments, we picked young-adult hermaphrodites with ≤ 2 visible eggs in their uterus. OH16230 were washed in M9 buffer containing 1 mM tetramisole hydrochloride to minimize motion, then placed in CTX buffer and loaded into the microfluidic chip (Larsch et al., 2013). For each animal, we first obtained a highresolution 4-color landmark volume for neuronal identification. We then observed a 2-minute unilluminated waiting period to allow the animal to recover from its exposure to laser light. Lastly, we performed a 4-minute, single-channel recording to capture nuclear GCaMP6s activity, at a frequency of ~4 Hz. We used a 488 nm laser to continuously excite GCaMP6s throughout the recording. Similar to previous experimenters (Zaslaver et al., 2015), we noted that the onset of the 488 nm laser correlates with neuronal activity and that this activity rapidly habituates toward a visible neuronal baseline. Thus, we waited 1-minute before delivering our chemical stimuli in this constant 488 nm laser background. In each experiment, we presented all three stimuli separated by 1-minute intervals. At the end of every minute, we presented a 10 s pulse of either 160mM NaCl, 10^{-4} 2-butanone, or 10^{-4} 2,3-pentanedione. Stimuli were presented in CTX buffer maintaining a constant pH 6 and 350 mOsm/L across stimulus and non-stimulus presentation. The order of stimulus presentation was rotated periodically to avoid sampling order-dependent stimulus responses.

Brainwide imaging of neuronal activity traces

After the whole-brain neuronal activity experiments concluded, we identified as many neurons as possible within the 4-color identification volumes. Neuronal identification was limited by our field of view (FOV), thus neurons like I1L/R and DB1 have fewer samples. Also, on occasion a few neurons that were furthest from the lens were too dim to identify, but due to the variety of animal orientations imaged in our microfluidic chip this small reduction in sampling was distributed between many neurons. We correlated identified neurons in the landmark volume to their GCaMP6s recordings, and extracted their traces (Table S6; https://zenodo.org/record/3906530) using deformable non-negative matrix factorization (dNMF) (Nejatbakhsh et al., 2020). To avoid any potential camera issues related to recording initiation and termination, we removed the first 1 s and last frame of every recording. To facilitate comparison of neuronal activity across animals, we downsampled recordings to the lowest frame rate observed within their group, 4 Hz for OH16230 heads and 3.87 Hz for OH16230 tails. $\Delta F/F_0$ was computed as follows: a) for ΔF we approximated the GCaMP6s bleach curve by fitting a 1st order exponential decay to each neuron, then subtracted this bleach curve from the neuron's activity trace; b) for Fo we calculated the 5th percentile for each neuron's activity trace; and c) ΔF/F₀ was computed, per neuron, as the ratio of these two values. Neurons within 5 µm distance of each other, whose traces showed at least 95% correlation, were deemed too similar and removed. Neurons with $N \le 3$ where not evaluated due to insufficient sampling. When comparing neuronal activity across animals, we used dNMF to normalize activity traces per neuron class. In the supplement we present similar experiments performed using OH15500 animals (Table S6; https://zenodo.org/record/3906530). For OH15500 we used DI water instead of CTX buffer, the three stimuli remained the same but NaCl was presented for 20 s at 200 mM, neuronal traces were extracted using a previous method that predates dNMF (https://github.com/venkatachalamlab/NeuroPAL-traces/) (Venkatachalam et al., 2016), and visual inspection was used to identify and remove traces from neighboring neurons that exhibited mixed signals. OH15500 heads were downsampled to 4.1 Hz.

QUANTIFICATION AND STATISTICAL ANALYSIS

Statistical analysis

Statistical details of experiments can be found in the following section. Statistical data is reported in the main text, figures, and tables as noted. For all statistical analyses, N represents the number of worms sampled. Significance adheres to the common standard, after adjusting for multiple testing, of p or $q \le 0.05$. The symbols *, **, ***, and **** refer to p or $q \le 0.05$, 0.01, 0.001, and 0.0001, respectively.

Mutant analysis

Statistical analysis of NeuroPAL-color alterations, for four neuron classes, in two pag-3(-) mutant backgrounds was Bonferroni corrected for eight tests (Figure 5B; Table S5). We used a One-Sided Fischer's Exact Test to analyze mutant-induced changes in PVR, VA2, and VB3. We used a One-Sided Rank Sum Test to analyze mutant-induced changes in AVE, scoring 0 if no changes were observed, 1 if either AVEL or AVER was altered, and 2 if both AVE neurons were altered. Statistical analysis of NeuroPAL color loss and UNC-25 reporter loss, for the RMED and RMEV neurons, in two eor-1(-) mutant backgrounds was Bonferroni corrected





for eight tests (Figures 5F and 5G; Table S5). We used a One-Sided Fischer's Exact Test to analyze mutant-induced loss of RMED/V blue coloring in NeuroPAL. We used a One-Sided Rank Sum Test to analyze mutant-induced changes in the RMED/V UNC-25 reporter expression, scoring 0 if expression was lost, 1 if expression was weak but visible, and 2 if no changes were observed. Mutant analysis studies were not blinded.

Analysis of brainwide imaging data

To analyze the whole-brain imaging stimulus responses (Figures 6, S1H, and S2; Table S6), we reviewed ASE responses to salt and AWC responses to the odors - the primary sensory neurons for these stimuli. Worms were marked as stimulus responsive if either their left or right neuron showed the published response to their corresponding stimuli (ASE excitation for NaCl and AWC inhibition for odors) (Chalasani et al., 2007; Suzuki et al., 2008). 21 heads responded to all three stimuli, providing strong internal controls to compare their circuit activity across all stimuli. Additionally, 21 tails were included, without response verification as the heads of these animals were not simultaneously imaged. Premotor interneurons (AVA, AVB, AVD, AVE, PVC) and ventral-cord motor neurons (AS, DA, DB, DD, VA, VB, VC, VD) show spontaneous cyclical activity and thus were excluded from significance testing. For testing that did not compare asymmetries, left/right neuron pairs from the same class were combined; thus the maximum sample size for these tests is either 42 left/right neuron pairs (e.g., AFDL and AFDR) or 21 single-sided neurons (e.g., I6). We used t tests (2-tailed, paired) to compare the mean signal during stimulus presentation with an identical period immediately prior, within the very same neuron (a strong internal control). These p values were corrected for multiple testing using false discovery rate (FDR) adjusted q-values (Storey, 2002). Post-stimulus responses were identified by first ensuring the neuron's mean stimulus response exceeded its pre-stimulus mean (to avoid mistaking repolarizing calcium activity for a post-stimulus response), then testing whether the post-stimulus mean exceeded the mean stimulus response (1-tailed, paired t test). Post-stimulus p values were corrected using FDR. To test asymmetric neuron responses we used 2-tailed, two-sample (unpaired) t tests.

Statistical analysis software

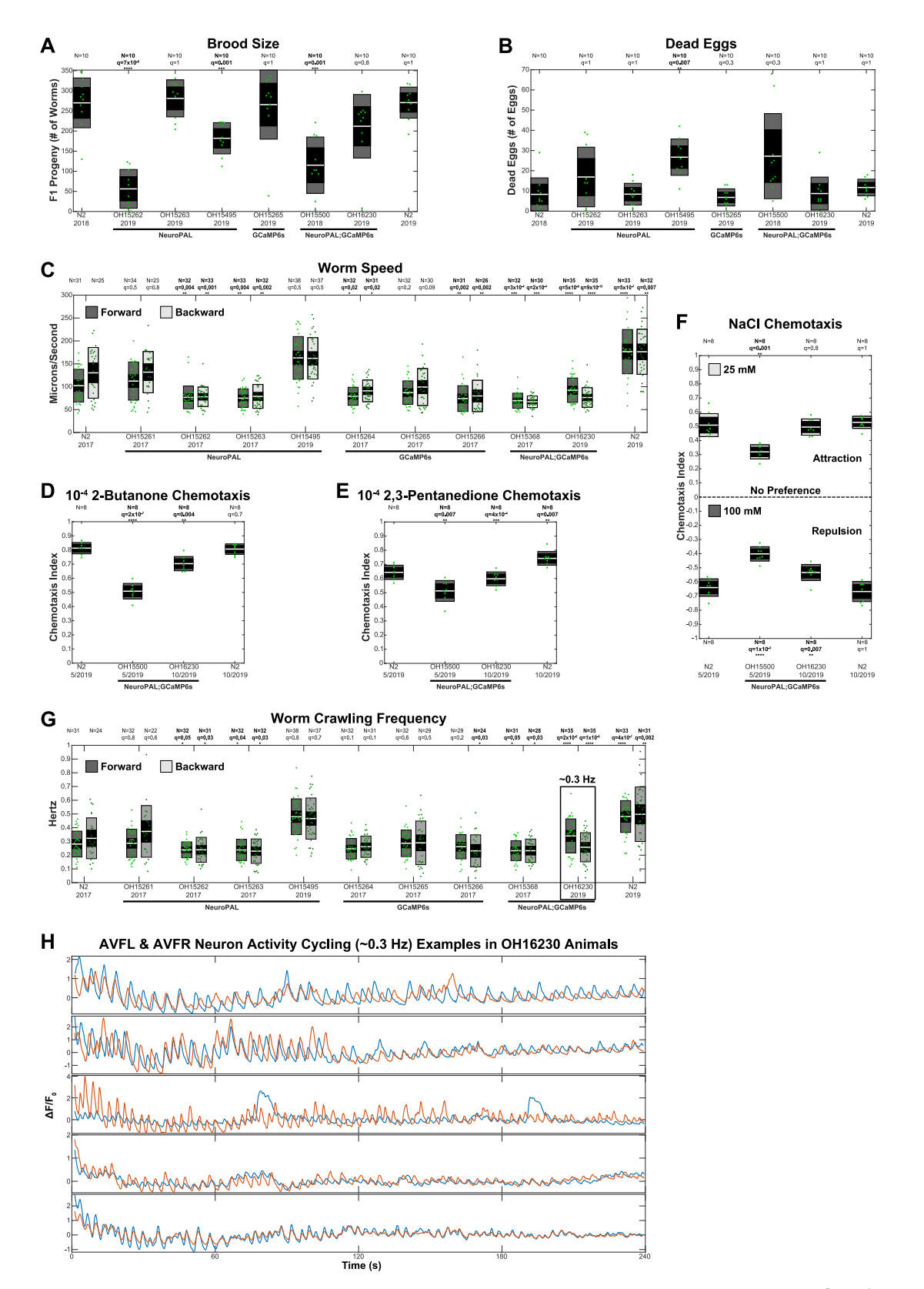
All statistics and code were run in MATLAB, using standard toolboxes, with the exception of the OME Bio-Formats API (used to read in Zeiss CZI and Nikon ND2 file formats) (Linkert et al., 2010), dNMF (used to extract whole-brain calcium activity) (Nejatbakhsh et al., 2020), MATLAB geometry toolbox for 2D/3D geometric computing (https://github.com/mattools/matGeom), and MathWorks File Exchange functions (Methods S1).

Additional Resources

NeuroPAL imaging can be performed using a wide variety of microscopes, as further detailed in the manual "Configuring Your Microscope for NeuroPAL." Manuals for microscope setups and cell identification are available online at: https://www.hobertlab.org/ neuropal/.



Supplemental Figures











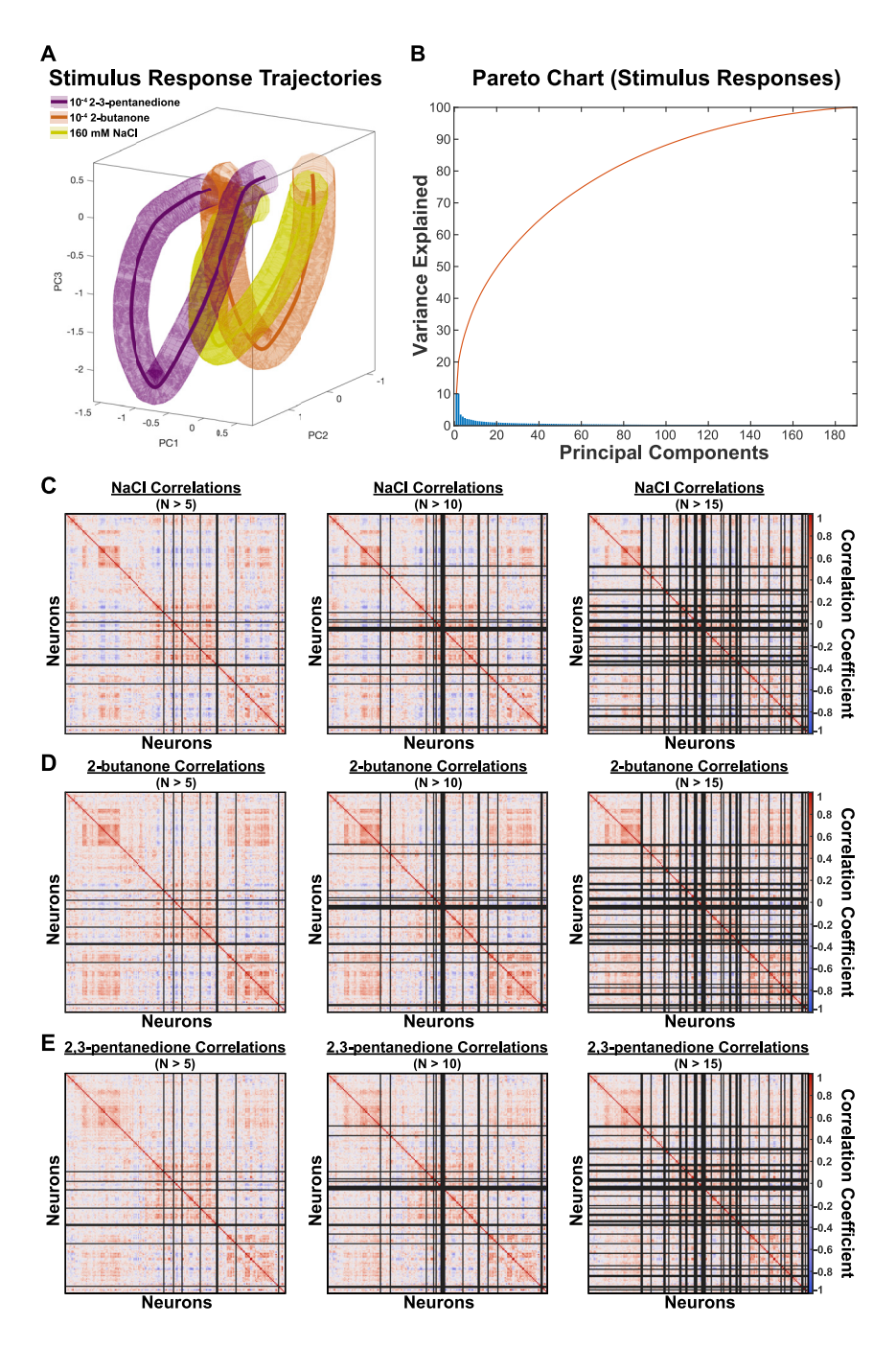


Figure S2. Whole-Brain Neuronal Dynamics and Pairwise Neuronal Correlations in Response to Chemosensory Stimuli, Related to Figure 6

(A) Average phase trajectories (N = 21 animal heads) of whole-brain neuronal activity in response to stimuli (10 s of stimulus application and 20 s thereafter). Trajectories are presented for 160 mM NaCl (yellow), 10^{-4} 2-butanone (orange), and 10^{-4} 2-3-pentanedione (purple), with the standard error of the mean shown as a mesh. The axes shown are the first three principal components of whole-brain activity. The average stimulus trajectories exhibit similarities but remain distinguishable.

(B) The Pareto chart of variance explained per principal component.

(C–E) Average pairwise correlations between 189 neurons in the 30 s following onset of (C) NaCl, (D) 2-butanone, and (E) 2,3-pentanedione. All correlation maps are presented on the same axes, determined by clustering the full-time-course correlations, then thresholded for sample sizes of N > 5, 10, and 15 neurons. The set of correlated and anti-correlated neurons differs for each stimulus presentation.



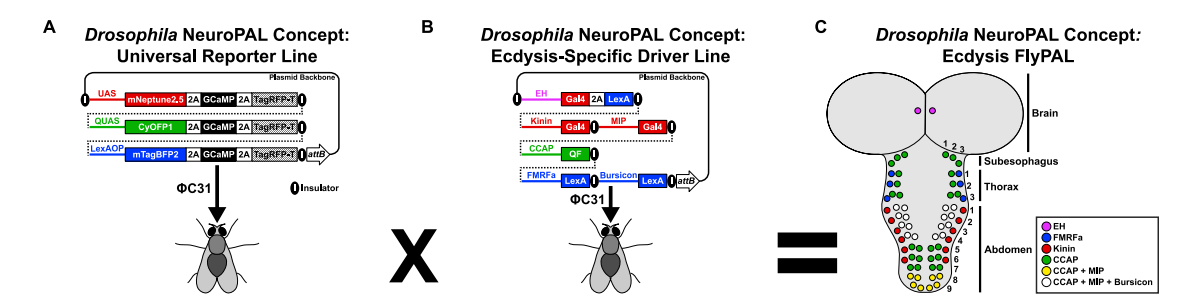


Figure S3. A Drosophila FlyPAL Design Concept, Related to Figures 1 and 7

(A) A "Universal-Reporter Line" for flies employing three orthogonal binary-expression systems to independently drive each of the three NeuroPAL landmark fluorophores (Brand and Perrimon, 1993; Kakidani and Ptashne, 1988; Lai and Lee, 2006; Potter et al., 2010). Optional T2A sequences enable co-expression of GCaMP6s and TagRFP-T to facilitate ratiometric calcium imaging. Genetic insulators are used to insulate the expression of each landmark fluorophore. ΦC31 integration is used to integrate this transgene into the fly genome.

(B) An "Ecdysis-Specific Driver Line" employs five short enhancer fragments to drive expression of the NeuroPAL landmark fluorophores using their corresponding binary systems (Diao et al., 2017; Kim et al., 2006).

(C) Crossing the Universal Reporter and Ecdysis-Specific Driver lines generates an "Ecdysis FlyPAL" wherein ecdysis-specific neurons can be identified by their color and position. Ecdysis-specific neurons can then be individually identified in calcium activity recordings.